

**STUDY OF HIERARCHICAL POROUS CARBONS AND ITS COMPOSITES  
AS FUEL CELL CATALYST SUPPORTS**

A Thesis

Presented to the Faculty of the Graduate School  
of Cornell University

In Partial Fulfillment of the Requirements for the Degree of  
Master of Science

by

Yu-Han Tsai

August 2021

© 2021 Yu-Han Tsai

## ABSTRACT

Engineering the type and size of porosity in carbon catalyst supports used in membrane electrode assemblies of fuel cells has attracted great interest recently. The effort is motivated by the goal of improved electrocatalyst dispersion, long-term chemical stability, and facilitated fuel flow. To date, various carbon catalyst supports including carbon black, graphene, and carbon nanotubes have been studied, yet efforts are still being made to investigate novel catalyst supports for enhanced fuel cell performance.

In this work, I conducted a systematic study using hierarchical porous carbons (HPCs) as fuel cell catalyst supports to understand the effect of porosity on fuel cell performance. HPCs combine into a single material platform three different kinds of porosity: macropores ( $> 50$  nm), mesopores ( $2 - 50$  nm), and micropores ( $< 2$  nm). By modifying the ice-templating method developed previously in the Giannelis group, the size of mesopores with high fidelity could be controlled. HPCs featuring high surface area ( $> 1000$  m<sup>2</sup>/g) and pore volume ( $\sim 2.3$  cm<sup>3</sup>/g), moderate electrical conductivity ( $\sim 1$  S/cm), with different mesopore size ranging from 4 nm to 20 nm were demonstrated. To further increase the electrical conductivity without altering the hierarchical porous structure, carbon additives such as graphene nanoplatelets (GN) and carbon nanotubes into HPCs were introduced. In addition, the effect of post thermal treatment was investigated. The resulting composite material (HPCs-GN) shows a surface area 2 times higher than that of Vulcan XC-72 with comparable electrical conductivity. Finally, microscopy images demonstrate smaller average nanoparticle size of platinum (Pt) supported on HPCs even at high catalyst loading (40 wt%) compared with commercial Pt on Vulcan XC-72.

## BIOGRAPHICAL SKETCH

Yu-Han (Joseph) Tsai was born and raised in the capital of Taiwan, Taipei City, one of the metropolitan cities in Northeast Asia. He lived in a happy family with his parents and three sisters, and spent most of his childhood with his grandma. As most of the Taiwanese students, Yu-Han focused on his studies when he was a teenager and explored his career interest along the way. Yu-Han was fascinated with science at a very young age and enjoyed conducting simple experiments that helped to explain any scientific phenomenon under the guidance of his teachers.

His interest in materials science stemmed from his experience performing independent research as a college student at Academia Sinica, one of the government-led renowned research institutes in Taiwan. He chose to major in materials science at National Taiwan University (NTU), the highest ranked university in Taiwan, to construct a robust foundation of theoretical knowledge and learned cutting-edge scientific advancements worldwide. Yu-Han combined his learnings from school with his undergraduate research and managed to carry out experiments that resulted in scientific discoveries and publications in the field of biointerface materials.

Equipped with basic experimental skills and knowledge concerning scientific research, Yu-Han decided to follow his passion and delved into the energy-related research, pursuing his graduate studies at Cornell University after his graduation from NTU. At Cornell, Yu-Han joined Professor Emmanuel P. Giannelis' research group, where he had the opportunity to work and learn from outstanding researchers and scholars. Many friendly and kind graduate students and postdocs have helped him in terms of research and built lifelong friendship with him. Also, Yu-Han was greatly inspired by his advisor who always enlightened him with guidance and invaluable suggestions.

During his two-year master's program, Yu-Han was also fortunate to collaborate with other students and postdocs in the Center for Alkaline-based Energy Solutions (CABES), where he formulated comprehensive understanding concerning the topic of fuel cells in various aspects, including catalysts, supports, membranes, and theoretical computations. His research was focused on exploring novel catalyst supports using hierarchical porous carbons (HPCs). Yu-Han has demonstrated the great potential of utilizing HPCs as a novel catalyst support. This project allowed Yu-Han to familiarize himself with the fuel cell related research and led to his future PhD studies at UCLA.

Currently, Yu-Han has come back to Taiwan. He led a wonderful life at Cornell and he will miss his friends dearly. Yu-Han hopes to apply his learnings from his master's research into his PhD studies and to make further contributions to the research of fuel cells.

Dedicated to all the people who have helped me during my master's studies at Cornell and also to my friends and family: for always encouraging me and supporting me.

## ACKNOWLEDGEMENTS

First, I would like to express my deepest gratitude to my parents, Sung-Chi Tsai and Ying-Hui Lin, for their love, support, and trust in my life. They have taught me to always strive for the best and to be responsible for myself. I would also like to thank my sisters and my grandma, Pei-I Tsai, Pei-Chia Tsai, Pei-Ying Tsai, and Lin-Rong Tsai, for always be there for me throughout my master's studies. To my beloved uncle Lun-Chien Lin, thank you for always encouraging me to pursue my dream and to follow my passion. I will forever remember the invaluable life lessons that you taught me of becoming a better version of myself.

I would also like to acknowledge my advisor, Professor Emmanuel Giannelis, who has always been kind and patient during my two-year studies at Cornell. He inspired me through his words of advice in many aspects that shaped me as a better researcher. I was fortunate to be his student and part of the group. His guidance was immensely appreciated.

To my committee member, Professor Jin Suntivich, thank you for organizing the monthly supports thrust meetings, in which I learned to work coherently and shared common goals with other like-minded researchers.

To my collaborator to the work presented in this thesis, who is also my mentor, Dr. Georgia Potsi, thank you for the numerous discussions that were crucial to all the breakthroughs in this project. I am also deeply grateful for your advice on my career development.

To all group members, you are all incredibly kind people whom I enjoyed doing research with very much. It was a pleasure to work with you all.

## TABLE OF CONTENTS

Biographical Sketch.....	iii
Dedication.....	v
Acknowledgements.....	vi
Table of Contents.....	vii
List of Figures.....	ix
List of Tables.....	xii
<b>1. INTRODUCTION.....</b>	<b>1</b>
1.1 Introduction to Fuel Cells .....	1
1.1.1 Introduction to Fuel Cell Catalyst Supports.....	6
1.1.2 Comparison between Different Carbon Catalyst Supports .....	7
1.1.3 Support Structure and Pore Size Effect on Fuel Cell Performance .....	10
REFERENCES .....	12
<b>2. FABRICATION OF HIERARCHICAL POROUS CARBONS WITH DIFFERENT MESOPORE SIZE AS FUEL CELL CATALYST SUPPORTS .....</b>	<b>15</b>
2.1 Introduction to Mesoporous Carbons and Hierarchical Porous Carbons .....	15
2.2 Synthetic Pathways of Hierarchical Porous Carbons .....	16
2.2.1 Hard-templating Methods .....	16
2.2.2 Soft-templating Methods .....	17
2.2.3 Ice-templating Methods .....	18
2.3 Experimental Section .....	20
2.3.1 Materials .....	20
2.3.2 Synthetic Procedure of HPCs with Different Mesopore Size .....	20
2.3.3 Post Thermal Treatment for Improved Electrical Conductivity .....	22
2.4 Characterization .....	23
2.5 Results and Discussions .....	23
2.5.1 Comparison of HPC-12-1-0 Before and After Thermal Treatment .....	23
2.5.2 Structural Investigation of HPCs with Different Mesopore Size Before and After Thermal Treatment .....	29
2.5.3 Elemental Analysis of HPCs with Different Mesopore Size .....	32
REFERENCES .....	33
<b>3. BALANCING SURFACE AREA AND ELECTRICAL CONDUCTIVITY OF HIERARCHICAL POROUS CARBONS – GRAPHENE NANOPATELETS COMPOSITES AS NOVEL FUEL CELL CATALYST SUPPORTS .....</b>	<b>36</b>
3.1 Introduction .....	36



3.2 Experimental Section .....	38
3.2.1 Materials .....	38
3.2.2 Synthetic Procedure of HPCs-GN Composites.....	38
3.2.3 Post Thermal Treatment for Improved Electrical Conductivity .....	39
3.3 Characterization .....	40
3.4 Results and Discussions .....	40
3.4.1 Comparison between Composite HPCs with Different Carbon Additives .....	40
3.4.2 Structural Analysis of HPCs-GN Composites .....	44
3.4.3 Compositional Analysis of HPCs-GN Composites .....	49
REFERENCES .....	55
<b>4. STUDY OF ELECTROCATALYST SUPPORTED ON HPCs WITH DIFFERENT MESOPORE SIZE AND HPCs-GN COMPOSITES .....</b>	<b>57</b>
4.1 Introduction .....	57
4.2 Experimental Section .....	59
4.2.1 Materials .....	59
4.2.2 Electrocatalyst Deposition on HPCs with Different Mesopore Size and HPCs-GN Composites .....	59
4.3 Characterization .....	60
4.4 Results and Discussions .....	61
4.4.1 Thermogravimetric Results for Electrocatalyst Loading Quantification of Pt-supported on HPCs with Different Mesopore Size and HPCs-GN Composites .....	61
4.4.2 Nanoparticle Size Distribution of Pt-supported on HPCs with Different Mesopore Size and HPCs-GN Composites .....	63
4.4.3 Structural Investigation after Pt deposition .....	67
REFERENCES .....	70

## LIST OF FIGURES

<b>1.1:</b> Schematic representation of a conventional fuel cell employing a proton conducting electrolyte. Protons are created via electro-oxidation of $H_2$ at the anode and then migrate across the electrolyte membrane to participate in the electro-reduction of $O_2$ at the cathode. Electrical energy is generated from the flow of electrons through the external circuit for charge balance. <sup>[5]</sup> .....	<b>3</b>
<b>1.2:</b> Configuration of a typical MEA. Each electrode comprises an MPS (macroporous substrate), which serves as the gas diffusion layer, an MPL made of carbon nanoparticles, and the CL made of catalyst nanoparticles supported on a carbon support. The two electrodes are separated by a polymer electrolyte membrane. <sup>[12]</sup> .....	<b>5</b>
<b>1.3:</b> SEM images of common carbon catalyst supports: (a) carbon black (Vulcan XC-72) (b) multi-walled carbon nanotubes (c) graphene nanoplatelets. ....	<b>8</b>
<b>1.4:</b> SEM image of commercial 40 wt% Pt nanoparticles supported on Vulcan XC-72. ....	<b>12</b>
<b>2.1:</b> Schematic showing the basic steps of ice-templating method to fabricate HPCs. The four steps are shown clockwise starting from the bottom left. <sup>[11]</sup> .....	<b>19</b>
<b>2.2:</b> Schematic representation of the ice-templating combined with hard-templating method to produce HPCs. ....	<b>22</b>
<b>2.3:</b> (a) SEM images of HPC-12-1-0 and HPCg-12-1-0 (b) AFM measurements of HPC-12-1-0 and HPCg-12-1-0. ....	<b>24</b>
<b>2.4:</b> (a) Pore size distribution, PSD, for HPC-12-1-0 and HPCg-12-1-0 obtained by mercury porosimetry (b) PSD of HPC-12-1-0 and HPCg-12-1-0 obtained by nitrogen sorption (c) Raman spectra of HPC-12-1-0 and HPCg-12-1-0. ....	<b>25</b>
<b>2.5:</b> XPS spectra of HPC-12-1-0 and HPCg-12-1-0. Vulcan XC-72 is also included for comparison. (a) Survey scan of HPC-12-1-0 (b) high-resolution scan of HPC-12-1-0 (c) survey scan of HPCg-12-1-0 (d) high-resolution scan of HPCg-12-1-0 (e) survey scan of Vulcan XC-72 (f) high-resolution scan of Vulcan XC-72.....	<b>27</b>
<b>2.6:</b> Energy Dispersive Spectra, EDS, and atomic percentage of HPC-12-1-0 and HPCg-12-1-0. Vulcan XC-72 is included for comparison. (a) HPC-12-1-0 (b) HPCg-12-1-0 (c) Vulcan XC-72.....	<b>28</b>

<b>2.7:</b> (a) Isotherms of HPCs with different mesopore size before and after thermal treatment (b) PSD of HPCs with different mesopore size before and after thermal treatment (c) – (h) SEM images of HPCs with different mesopore size before and after thermal treatment (c) HPC-4-1-0 (d) HPCg-4-1-0 (e) HPC-12-1-0 (f) HPCg-12-1-0 (g) HPC-20-1-0 (h) HPCg-20-1-0. ....	<b>31</b>
<b>2.8:</b> EDS of HPCs with different mesopore size before thermal treatment. (a) HPC-4-1-0 (b) HPCg-4-1-0 (c) HPC-12-1-0 (d) HPCg-12-1-0 (e) HPC-20-1-0 (f) HPCg-20-1-0. ....	<b>33</b>
<b>3.1:</b> Schematic representation of the ice-templating combined with hard-templating to produce HPCs-GN or HPCs-MWCNT composites. ....	<b>41</b>
<b>3.2:</b> SEM images of different HPCs composites at low and high magnification. (a,b) HPCs-GN (c,d) HPCs-MWCNT (e,f) HPCs-ox-MWCNT. ....	<b>43</b>
<b>3.3:</b> Surface area and electrical conductivity of HPCs-GN containing various amounts of GN. ....	<b>45</b>
<b>3.4:</b> (a) Isotherms and (b) pore size distributions of HPCs-GN composites with different amounts of GN. ....	<b>46</b>
<b>3.5:</b> Surface area and electrical conductivity of HPCs-GN containing different amounts of GN after the step of thermal treatment. ....	<b>47</b>
<b>3.6:</b> (a) Isotherms of thermally-treated HPCs-GN composites containing different amounts of GNs (b) PSD. ....	<b>48</b>
<b>3.7:</b> XPS spectra of HPC-12-1-0 (pristine) and HPC-12-1-0 (40% GN). Vulcan XC-72 is included for comparison. (a) Survey scan of HPC-12-1-0 (pristine) (b) high-resolution scan of HPC-12-1-0 (pristine) (c) survey scan of HPC-12-1-0 (40% GN) (d) high-resolution scan of HPC-12-1-0 (40% GN) (e) survey scan of Vulcan XC-72 (f) high-resolution scan of Vulcan XC-72.....	<b>50</b>
<b>3.8:</b> XPS spectrum of thermally treated HPC-12-1-0 (pristine) and HPC-12-1-0 (40% GN). Vulcan XC-72 is included for comparison. (a) Survey scan of HPCg-12-1-0 (pristine) (b) high-resolution scan of HPCg-12-1-0 (pristine) (c) survey scan of HPCg-12-1-0 (40% GN) (d) high-resolution scan of HPCg-12-1-0 (40% GN) (e) survey scan of Vulcan XC-72 (f) high-resolution scan of Vulcan XC-72. ....	<b>52</b>
<b>3.9:</b> EDS spectra and atomic percentage of HPC-12-1-0 (pristine) and HPC-12-1-0 (40% GN). Vulcan XC-72 is included for comparison. (a) HPC-12-1-0 (pristine) (b) HPCg-12-1-0 (pristine) (c) HPC-12-1-0 (40% GN) (d) HPCg-12-1-0 (40% GN) (e) Vulcan XC-72.....	<b>54</b>

<b>4.1:</b> TGA results of supported electrocatalysts. (a) 40 wt% Pt/HPCg-4-1-0 (pristine) (b) 40 wt% Pt/HPCg-12-1-0 (pristine) (c) 40 wt% Pt/HPCg-20-1-0 (pristine) (d) 40 wt% Pt/HPCg-12-1-0 (40% GN) (e) commercial 40 wt% Pt/Vulcan XC-72.....	<b>62</b>
<b>4.2:</b> SEM images of Pt supported on different carbon supports. (a) 40 wt% Pt/HPCg-4-1-0 (pristine) (b) 40 wt% Pt/HPCg-12-1-0 (pristine) (c) 40 wt% Pt/HPCg-20-1-0 (pristine) (d) 40 wt% Pt/HPCg-12-1-0 (40% GN) (e) commercial 40 wt% Pt/Vulcan XC-72. ....	<b>64</b>
<b>4.3:</b> BSE images of Pt supported on different carbon supports and the resultant Pt PSD diagrams. (a) 40 wt% Pt/HPCg-4-1-0 (pristine) (b) 40 wt% Pt/HPCg-12-1-0 (pristine) (c) 40 wt% Pt/HPCg-20-1-0 (pristine) (d) 40 wt% Pt/HPCg-12-1-0 (40% GN) (e) Commercial 40 wt% Pt/Vulcan XC-72. The fitting curve in each PSD diagram is included based on the histogram. ....	<b>66</b>
<b>4.4:</b> (a) BET surface area comparison of HPCs with different mesopore size and HPCs-GN, before and after Pt deposition (b) isotherms of HPCs with different mesopore size and HPCs-GN, before and after Pt deposition (c) pore size distribution of HPCs with different mesopore size and HPCs-GN, before and after Pt deposition. Vulcan XC-72 before and after Pt deposition are included for comparison. ....	<b>69</b>

## LIST OF TABLES

<b>1.1:</b> Fuel cell types and selected features. <sup>[5]</sup> .....	<b>4</b>
<b>2.1:</b> Surface area, pore volume, and electrical conductivity of HPCs with different mesopore size before thermal treatment. ....	<b>29</b>
<b>2.2:</b> Surface area, pore volume, and electrical conductivity of HPCs with different mesopore size after thermal treatment. ....	<b>30</b>
<b>3.1:</b> Materials and compact characteristics. <sup>[6]</sup> .....	<b>37</b>
<b>3.2:</b> Surface area, pore volume, and electrical conductivity of composite HPCs with different carbon additives. Vulcan XC-72 is included for comparison. ....	<b>44</b>
<b>3.3:</b> Pore volume of composite HPCs with different amounts of GN before and after thermal treatment. Vulcan XC-72 and a sample of pure graphene nanoplatelets are included for comparison. ....	<b>48</b>
<b>4.1:</b> Pore volume of HPCs with different mesopore size and HPCs-GN before/after Pt deposition. Vulcan XC-72 before and after Pt deposition are included for comparison. ....	<b>68</b>

## CHAPTER 1

### INTRODUCTION

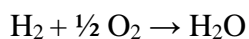
Traditional fossil fuels such as coal, petroleum, and natural gas are all non-renewable resources, the mass consumption of which has resulted in the global energy crisis, undermining the world economy and ecology. The irreversible effects of utilizing fossil fuels have driven scientists to explore more environmentally-friendly energy resources. U.S. has recently arrived at a crossroads where renewable energy technologies such as wind, solar, and hydropower are economically competitive with conventional fossil fuels.<sup>[1]</sup> Due to the unpredictability and the intermittence of renewable energies, to ensure sustainable energy supply, scientists have researched several cost-effective energy transformation technologies. Among them, systems for the storage and conversion of electrochemical energy, such as batteries, supercapacitors, and fuel cells have attracted great interest, since they are considered a sustainable and environmentally-friendly solution.<sup>[2]</sup>

#### 1.1 Introduction to Fuel Cells

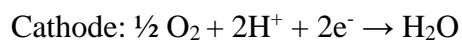
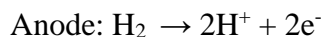
Fuel cells have emerged as attractive alternatives to conventional energy resources due to their potential of reducing environmental pollution and the greenhouse effect while maintaining high electrical energy conversion efficiency (up to 55 – 65%).<sup>[3]</sup> From an environment-protection perspective, since transportation tops other sectors, including the electric power, agricultural, and residential industries in terms of carbon dioxide emission, the adoption of fuel cells can meet the energy demand for combustion engine powered vehicles, while significantly reducing carbon

dioxide emissions.<sup>[4]</sup> Another major advantage of fuel cell technology is its modular and distributed nature, which can be beneficial for a wide range of energy-related applications, including systems as small as portable devices and as large as transportation.<sup>[5,6]</sup> Because fuel cell technology does not require centralized grid systems for energy distribution, it can also solve the energy predicament encountered in remote regions or rural areas.

A fuel cell is an electrochemical device that converts the energy of a chemical reaction into electrical energy. Figure 1.1 demonstrates the primary components of a typical fuel cell – a cathode, an anode, and an ion conducting electrolyte. A fuel such as hydrocarbon or hydrogen gas is fed into the anode and an oxidant, usually oxygen or oxygen-containing air, is brought into the cathode compartment.<sup>[5]</sup> Due to the potential difference between the anode and the cathode, a chemical driving force is generated for the hydrogen and oxygen to react to produce water according to the following chemical reaction:



The design principle of a fuel cell is to divide the aforementioned chemical reaction into two half-cell reactions by introducing an electrolyte, which serves as a barrier that separates the fuel at the anode and the oxidant at the cathode. The half-cell reactions are presented below:



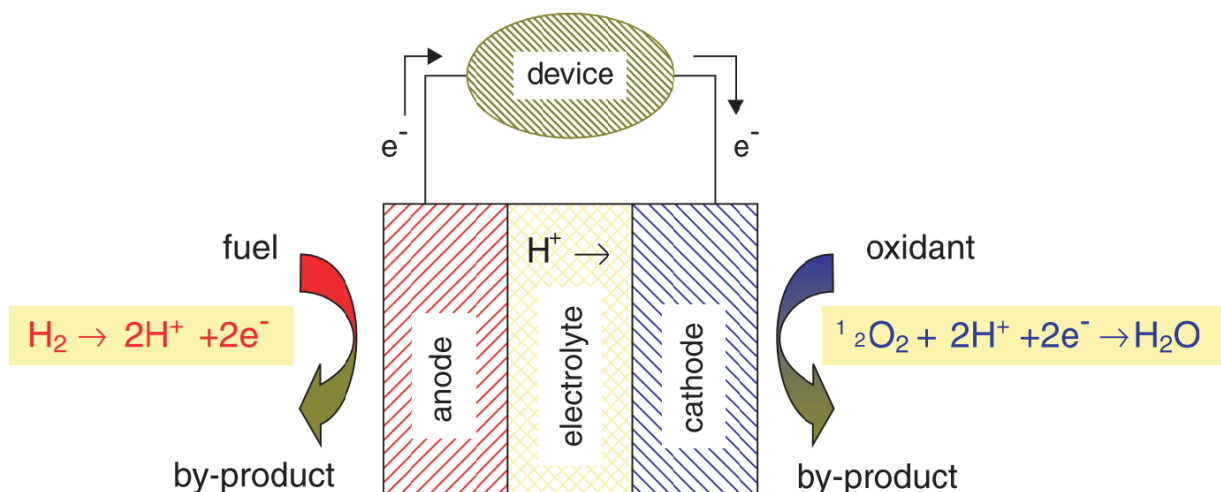


**Figure 1.1:** Schematic representation of a conventional fuel cell employing a proton conducting electrolyte. Protons are created via electro-oxidation of  $\text{H}_2$  at the anode and then migrate across the electrolyte membrane to participate in the electro-reduction of  $\text{O}_2$  at the cathode. Electrical energy is generated from the flow of electrons through the external circuit for charge balance.<sup>[5]</sup>

Fuel cells are conventionally categorized based on their electrolyte material.<sup>[7]</sup> Because ion conduction is a thermally activated process, the magnitude of which varies from one material to another, the type of electrolyte will determine the fuel cell's operation temperature. In general, the higher temperatures are preferred for enhanced performance, whereas lower temperature is desired for practical applications. State-of-the-art fuel cell technologies are listed in Table 1.1. Among them, polymer electrolyte membrane (or proton exchange membrane) fuel cells (PEMFCs) have the widest range of applications due to their relatively low operation temperature, high power density and energy conversion efficiency. However, the severe dependence on costly platinum catalysts used in PEMFCs still impedes large-scale production. Alkaline fuel cells (AFCs), on the other hand, are drawing interest because of their improved oxygen reduction kinetics, as well as



the ability to utilize catalysts that are either free of platinum-group-metals (PGM) or contain relatively small amounts of PGMs.<sup>[8,9]</sup>

**Table 1.1:** Fuel cell types and selected features.<sup>[5]</sup>

Type	Temperature °C	Fuel	Electrolyte	Mobile Ion
PEM*: polymer electrolyte membrane	70-110	H <sub>2</sub> CH <sub>3</sub> OH	Sulfonated polymers (Nafion™)	(H <sub>2</sub> O) <sub>n</sub> H <sup>+</sup>
AFC: alkali fuel cell	100-250	H <sub>2</sub>	Aqueous KOH	OH <sup>-</sup>
PAFC: phosphoric acid fuel cell	150-250	H <sub>2</sub>	H <sub>3</sub> PO <sub>4</sub>	H <sup>+</sup>
MCFC: molten carbonate fuel cell	500-700	hydrocarbons CO	(Na,K) <sub>2</sub> CO <sub>3</sub>	CO <sub>3</sub> <sup>2-</sup>
SOFC: solid oxide fuel cell	700-1000	hydrocarbons CO	(Zr,Y)O <sub>2-δ</sub>	O <sup>2-</sup>
* also known as proton exchange membrane				

Progress regarding fuel cell research is not only made in increasing power density and energy conversion efficiency but also in various preparation techniques and materials for fabrication. Some of the mainstream preparation procedures include: (1) indirect decal method, (2) gas diffusion layer (GDL)-based method, and (3) membrane-based method.<sup>[10]</sup> The membrane-based method in which membrane electrode assembly (MEA) is manufactured is generally adopted to

fabricate AFCs. Developed based on the concept of a conventional fuel cell, a typical MEA (shown in Figure 1.2) usually consists of two electrodes, the anode and cathode, which are separated by a polymer electrolyte membrane, most commonly Nafion. The electrodes are composed of several layers, which have been designed to provide the best fuel flow and electrical conductivity, while maintaining the capability of water and thermal management.<sup>[11]</sup> To be more specific, a typical MEA comprises a macroporous layer, serving as the gas diffusion layer (GDL) made of carbon fibers coated with hydrophobic polytetrafluoroethylene (PTFE), a microporous layer (MPL) containing carbon nanoparticles, and the catalyst layer (CL) made of electrocatalyst nanoparticles deposited on a carbon support, which is in direct contact with the Nafion polyelectrolyte membrane.<sup>[12]</sup> The research of this thesis will center on engineering the carbon support of AFCs for better fuel cell performance.

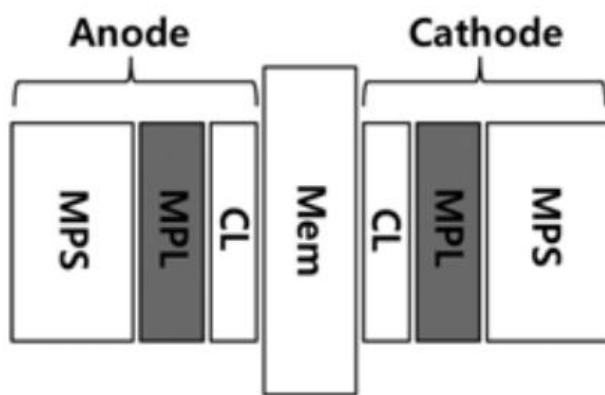


**Figure 1.2:** Configuration of a typical MEA. Each electrode comprises an MPS (macroporous substrate), which serves as the gas diffusion layer, an MPL made of carbon nanoparticles, and the CL made of catalyst nanoparticles supported on a carbon support. The two electrodes are separated by a polymer electrolyte membrane.<sup>[12]</sup>

### 1.1.1 Introduction to Fuel Cell Catalyst Supports

One of the major problems that hinders the widespread commercialization of fuel cell technology is the utilization of expensive PGM as electrocatalysts inside MEA. To that end, a decrease or even elimination of PGM while maintaining the fuel cell performance becomes a critical issue for fuel cell research. There are two main research directions to accomplish this goal. One is through the adoption of non-noble catalysts, and the other is to improve the utilization of catalysts by enhancing their activity.<sup>[13,14]</sup> For the latter, it is usually achieved by introducing a catalyst support which serves as a substrate to support highly dispersed catalysts, leading to increased reactive surface area. The design principles for such supports derived from the above-mentioned concept are as follows: (1) high surface area for catalyst dispersion, (2) high porosity for facilitated fuel flow, (3) high electrical conductivity for charge transport, and (4) long-term chemical stability during fuel cell operation.<sup>[15]</sup> The most common supports that meet the above requirements are carbon based materials such as carbon black, carbon nanotubes/fibers, and graphene/graphene oxide. Noncarbon supporting materials including metal, nitride, carbide, mesoporous silicas, and metal oxides, are also developed owing to their high chemical/electrochemical and thermal stability during fuel cell operation.<sup>[16]</sup> However, in terms of electrical conductivity, surface area, and homogeneous dispersion of catalytic nanoparticles, most carbon supports still outperform their noncarbon counterparts.

### 1.1.2 Comparison between Different Carbon Catalyst Supports

The geometry of the support significantly affects the fuel cell performance, since it influences not only the dispersion of the metal catalyst but also the flow of reactants. Figure 1.3 contains high-resolution scanning electron microscopy (SEM) images of different carbon supports. Carbon black is the most widely used carbon support due to ease of fabrication and its reasonable electrical conductivity and surface area. Vulcan XC-72, among all carbon black, is the commercial standard utilized in fuel cell research. From Figure 1.3 (a), it can be clearly seen that Vulcan XC-72 features a spherical shape with a diameter less than 50 nm and forms aggregates easily. Vulcan XC-72 contains a large percentage (47%) of micropores (pore size less than 2 nm in diameter) inside its graphitic structure.<sup>[17]</sup> Despite Vulcan XC-72 being widely used in commercial fuel cells, the micropores within are suggested to be detrimental for fuel cell performance because they are not easily accessible to electrolyte.<sup>[18]</sup> The other main deficit of Vulcan XC-72 for fuel cell application is its insufficient electrochemical stability. During fuel cell operation, Vulcan XC-72 is easily oxidized at higher potential. In addition, the resulting degradation of the support increases in the presence of platinum (Pt) nanoparticles. This leads to the detachment of Pt from the support and the agglomeration of the Pt nanoparticles, which also contributes to the degradation of the catalyst.<sup>[19]</sup>

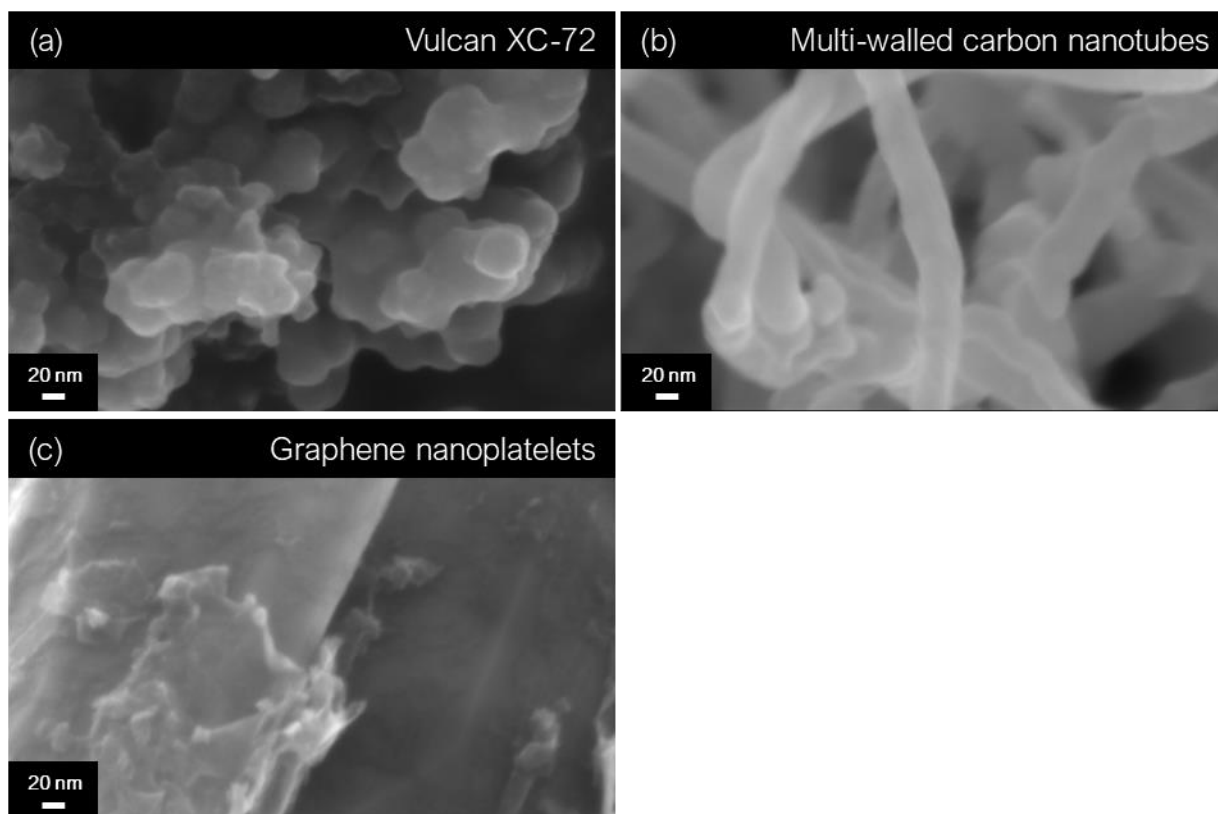


**Figure 1.3:** SEM images of common carbon catalyst supports: (a) carbon black (Vulcan XC-72) (b) multi-walled carbon nanotubes (c) graphene nanoplatelets.

In this context, new carbon allotropes as alternatives for catalyst supports have been widely studied for fuel cell application. Figure 1.3 (b) shows a typical structure of multi-walled carbon nanotubes (CNT). CNTs feature a unique tubular structure that provides high surface area, excellent electrical conductivity, and prolonged chemical stability, resulting in specific interactions between catalytic metals and the CNT supports. CNTs are free from deep cracks that contribute to low catalytic activity. The tubular structure also benefits mass transport when CNTs are incorporated into the catalyst layer of MEA. It is suggested that the structure of CNTs could ease the transportation of water and gas fuel, allowing the reactants to reach the catalyst surface easily.<sup>[19]</sup> Additionally, CNTs contain fewer impurities which are prone to poison metal catalysts when compared with

carbon black. However, due to their chemical inertness, CNTs without any surface modification lack binding sites, which are made of surface oxygen groups and are used to anchor catalyst nanoparticles, resulting in poor dispersion and agglomeration of the catalyst, especially at high loadings.<sup>[15]</sup> For real-world applications, the costly production of CNTs remains an issue. For example, CNTs are usually 200 times more expensive than graphene nanoplatelets.

Figure 1.3 (c) shows the surface morphology of graphene nanoplatelets (GN). The use of graphene as a catalyst support has been explored by growing numbers of researchers because it has high chemical stability and electrocatalytic ability, and above all, allows high catalyst loading.<sup>[19]</sup> Graphene also exhibits enhanced corrosion resistance compared with Vulcan XC-72 in the presence of catalysts.<sup>[20]</sup> This is due to the unique surface morphology of graphene that prevents the loss of electrochemical reactive surface area (ECSA) of the loaded catalysts, making graphene a more durable catalyst support than Vulcan XC-72. Similar to CNTs though, their inertness requires chemical modifications of the graphene surface to facilitate catalyst nanoparticle dispersion. The other main issue concerning graphene as a catalyst support is the tendency of easily lumping into multilayers, which can cause lowering of the surface area, thereby, decreasing the electrocatalytic activity of the supported catalysts.<sup>[19]</sup>

To conclude, although multiple carbon catalyst supports have been studied to date, there is still need for improvements in terms of optimizing the structure, chemical composition, surface functional groups, and porosity of carbon supports used inside the MEA of fuel cells. One strategy is the fabrication of composite carbon supports that take advantage of the individual material properties. For example, Park et al. pioneered a design approach of adding a spacing material in the catalyst layer which consists of Pt nanoparticles supported on 2-D and high surface area graphene sheets.<sup>[21]</sup> The spacing material used was Vulcan XC-72, which upon addition, could

enhance exfoliation of graphene sheets deposited with Pt nanoparticles and increase the distance between graphene sheets. The carbon black added catalyst layer could provide more Pt nanoparticles covered with the ionomer in the membranes, resulting in the enhancement of Pt utilization and thereby increasing the ECSA of the supported electrocatalysts. Additionally, with appropriate amount of Vulcan XC-72 incorporated into the catalyst layer, the oxygen transport within the pores in the cathode was improved due to the increasing gas-phase void volume. Kaplan et al. adopted a similar concept and synthesized Pt nanoparticles supported on carbon black-reduced graphene oxide (CB-rGO).<sup>[22]</sup> The hybrid structure with moderate Vulcan XC-72 content prevented the restacking of graphene oxide layers, modified the array of graphene and provided more available catalytic sites for the reactions. The resulting composite material demonstrated enhanced fuel cell performance and higher catalytic activity than the support made of solely carbon black or reduced graphene oxide. The ratio of carbon black to reduced graphene oxide comprising the composite support was critical because higher amount of carbon black would block the Pt catalytic sites and lower the activity of the supported electrocatalysts.

### **1.1.3 Support Structure and Pore Size Effect on Fuel Cell Performance**

It can be inferred from the previous sections that structural and morphological characteristics of the support significantly affect the electrochemical performance of the catalyst during fuel cell operation. Traditional carbon-based materials containing mainly micropores such as carbon nanotubes, graphene, and carbon black have attracted broad attention due to their versatile applications and have been extensively studied as fuel cell catalyst supports.

One example of the effect on fuel cell performance exerted by the different structure of supports was described by Uchida et al. It was proposed that the relatively low ECSA of the Pt supported on carbon black could be attributed to the large portion of Pt nanoparticles located in the interior of the hollow carbon black, while other carbon supports featuring more smooth surfaces could provide more accessible Pt nanoparticles that led to enhanced performance.<sup>[23]</sup> Another geometrical effect originated from different carbon supports is shown in Figure 1.4. Figure 1.4 is a high-resolution SEM image of Pt supported on Vulcan XC-72. The Pt nanoparticles can be distinctively seen from the substrate carbon material. This Pt on Vulcan XC-72 configuration could pose another issue for optimal performance because particles supported on solid carbon black (Vulcan XC-72) are exposed to ionomer during fuel cell operation, leading to adsorption of ionomer on the Pt surface, reducing the catalytic activity in ORR by a factor of 2 - 4.<sup>[24]</sup> To address this problem, highly porous carbon supports, or high surface area carbons (HSC) are investigated as an alternative for Vulcan XC-72. Among current studies focusing on porous carbons, commercial porous carbon black, such as Ketjanblack, has been proved to be effective in terms of shielding internal catalyst particles from external ionomers by incorporating the catalyst particles into the mesopores (2 – 50 nm). Since the hydrodynamic size of ionomers in fuel cells is usually between 2 – 7 nm, by engineering appropriate sizes of mesopores within Ketjanblack to shield catalyst nanoparticles, the ionomers cannot have access to the catalyst particle surface and generate unfavorable side reactions to deteriorate the catalyst layer.<sup>[25]</sup> The mesoporous structure also protects catalyst particle coarsening by particle migration and coalescence. The recent discovery of the benefits from introducing mesopores to carbon supports opens a new avenue for catalyst support engineering. While the mesopore size of Ketjenblack cannot be precisely controlled with high fidelity, scientists are currently researching on tuning size of mesopores within carbon



catalyst supports for improved performance and prolonged fuel cell lifetime. This thesis will focus on controlling the porosity of carbon supports to improve fuel cell performance.

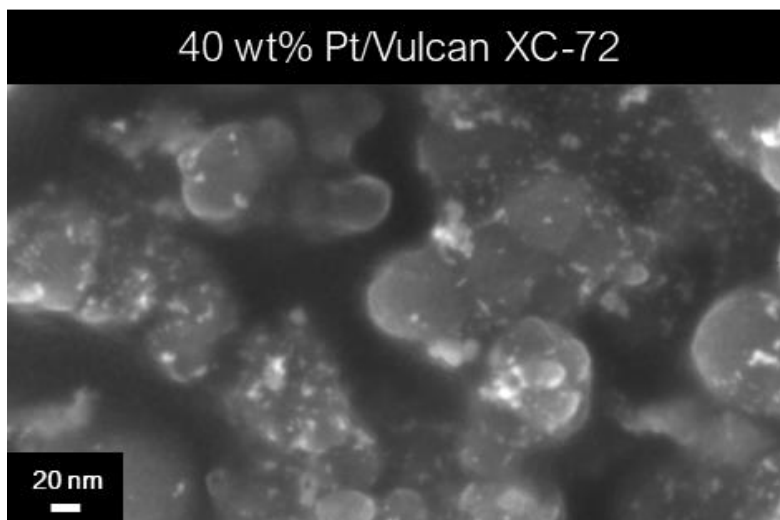


**Figure 1.4:** SEM image of commercial 40 wt% Pt nanoparticles supported on Vulcan XC-72.

## REFERENCES

- [1] M. Bolinger, J. Seel, D. Robson, **2019**.
- [2] M. Winter, R. J. Brodd, *Chem. Rev.* **2004**, *104*, 4245.
- [3] S. Mekhilef, R. Saidur, A. Safari, *Renew. Sustain. Energy Rev.* **2012**, *16*, 981.
- [4] U. S. Environmental Protection Agency, **2019**.
- [5] S. M. Haile, *Mater. Fuel Cells* **2003**, 24.
- [6] D. K. Niakolas, M. Daletou, S. G. Neophytides, C. G. Vayenas, *Ambio* **2016**, *45*, 32.
- [7] O. Z. Sharaf, M. F. Orhan, *Renew. Sustain. Energy Rev.* **2014**, *32*, 810.
- [8] H. A. Firouzjaie, W. E. Mustain, *ACS Catal.* **2020**, *10*, 225.

- [9] Z. Sun, B. Lin, F. Yan, *ChemSusChem* **2018**, *11*, 58.
- [10] T. Frey, M. Linardi, *Electrochim. Acta* **2004**, *50*, 99.
- [11] J. Hack, T. M. M. Heenan, F. Iacoviello, N. Mansor, Q. Meyer, P. Shearing, N. Brandon, D. J. L. Brett, *J. Electrochem. Soc.* **2018**, *165*, F3045.
- [12] S. Park, B. N. Popov, *Korean J. Chem. Eng.* **2014**, *31*, 1384.
- [13] P. Trogadas, T. F. Fuller, P. Strasser, *Carbon N. Y.* **2014**, *75*, 5.
- [14] Y. Yang, H. Peng, Y. Xiong, Q. Li, J. Lu, L. Xiao, F. J. Disalvo, L. Zhuang, H. D. Abrunã, *ACS Energy Lett.* **2019**, *4*, 1251.
- [15] E. Antolini, *Appl. Catal. B Environ.* **2009**, *88*, 1.
- [16] Y. J. Wang, D. P. Wilkinson, J. Zhang, *Chem. Rev.* **2011**, *111*, 7625.
- [17] B. Fang, J. H. Kim, M.-S. Kim, J. Yu, *Acc. Chem. Res.* **2013**, *46*, 1397.
- [18] K. Lee, J. Zhang, H. Wang, D. P. Wilkinson, *J. Appl. Electrochem.* **2006**, *36*, 507.
- [19] S. Samad, K. S. Loh, W. Y. Wong, T. K. Lee, J. Sunarso, S. T. Chong, W. R. Wan Daud, *Int. J. Hydrogen Energy* **2018**, *43*, 7823.
- [20] X. Zhou, J. Qiao, L. Yang, J. Zhang, *Adv. Energy Mater.* **2014**, *4*, 1301523.
- [21] S. Park, Y. Shao, H. Wan, P. C. Rieke, V. V. Viswanathan, S. A. Towne, L. V. Saraf, J. Liu, Y. Lin, Y. Wang, *Electrochem. commun.* **2011**, *13*, 258.
- [22] B. Yazar Kaplan, N. Haghmoradi, E. Biçer, C. Merino, S. Alkan Gürsel, *Int. J. Hydrogen Energy* **2018**, *43*, 23221.

- [23] Y. C. Park, H. Tokiwa, K. Kakinuma, M. Watanabe, M. Uchida, *J. Power Sources* **2016**, *315*, 179.
- [24] V. Yarlagadda, M. K. Carpenter, T. E. Moylan, R. S. Kukreja, R. Koestner, W. Gu, L. Thompson, A. Kongkanand, *ACS Energy Lett.* **2018**, *3*, 618.
- [25] M. Ko, E. Padgett, V. Yarlagadda, A. Kongkanand, D. A. Muller, *J. Electrochem. Soc.* **2021**, *168*, 024512.

## CHAPTER 2

# FABRICATION OF HIERARCHICAL POROUS CARBONS WITH DIFFERENT MESOPORE SIZE AS FUEL CELL CATALYST SUPPORTS

### 2.1 Introduction to Mesoporous Carbons and Hierarchical Porous Carbons

According to the International Union of Pure and Applied Chemistry (IUPAC), the following conventions are adopted to categorize different size of pores in a porous solid: micropores (pore diameter smaller than 2 nm), mesopores (pore diameter between 2 - 50 nm), and macropores (pore diameter larger than 50 nm).<sup>[1]</sup>

With growing numbers of publications elaborating the benefits of incorporating mesopores into catalyst supports, research concerning mesoporous carbons, another family of carbon-based materials, is attracting attention for their potential as catalyst supports. Their controllable and superior properties distinguish mesoporous carbons from traditional carbon-based materials in synthetic pathways, specific surface area and porosity, and interfacial properties.<sup>[2]</sup>

As discussed in Section 1.1.3, recent research regarding catalyst supports has focused on engineering appropriate size of mesopores within carbon supports for optimized fuel cell performance. Therefore, it is critical to construct a model system that features uniform and precisely controlled mesopore size, tunable surface functional groups, and simple synthetic approach. Hierarchical porous carbons (HPCs) appear as a suitable candidate due to controllable mesopore size and tunable material properties. HPCs possess a multimodal pore size distribution of micro-, meso-, and/or macropores, resulting in high specific surface area, short diffusion

distances, and high mass transfer rate.<sup>[3]</sup> Because of this combination, HPCs have been successfully incorporated into electrode materials for energy storage devices. In this chapter, the work on HPCs as model systems to understand how different size of mesopores will affect the carbon structure and material property is described.

## **2.2 Synthetic Pathways of Hierarchical Porous Carbons**

HPCs have been synthesized via various methods, including templating methods, templating/activation combined methods, and template-free methods.<sup>[3]</sup> Since templating methods are most used to design and fabricate HPCs, the following sections will introduce some of the common templating methods.

### **2.2.1 Hard-templating Methods**

Hard templating or nanocasting strategy is a well-studied method for direct synthesis of HPCs. Usually thermally stable inorganic solids, such as silica gel, silica nanoparticles,  $\text{Na}_2\text{CO}_3$ , and  $\text{Ni}(\text{OH})_2$  were chosen as hard templates.<sup>[3]</sup> Solid spherical templates, including silica particles and  $\text{Ni}(\text{OH})_2$ , would generate spherical pores within the substrate after template removal, whereas porous templates, such as silica gel, would create porous carbons with a 3D interconnected nanonetwork.<sup>[4–7]</sup> By varying preparation techniques, structural parameters, such as pore size, porosity, and pore volume, could be easily adjusted. Among different templating methods, the hard-templating methods provide the most accurate approach to fabricate HPCs with desired

nanopore size. For instance, Lei et al., synthesized mesoporous graphitized carbons with bimodal pore size distribution at 9.0 and 34.5 nm by selecting and mixing colloidal silica nanoparticles with 10 and 36 nm in diameter.<sup>[8]</sup> It was proposed from the experimental results that silica particles were faithfully replicated without significant aggregation during the synthesis. Derived from this concept, large-sized silica nanoparticles are appropriate if macropores are desired. The high fidelity in macro/meso-porous size control of HPCs grants hard-templating methods an unique advantage over any other templating method. Nevertheless, one of the main deficits of hard-templating methods is the utilization of stable inorganic solids that requires rigorous acid/base etching for template removal, which is relatively time-consuming and thus unsuitable for large-scale production.

### **2.2.2 Soft-templating Methods**

Soft-templating methods usually involve pre-synthesizing polymer templates such as phenolic resins and amphiphilic block copolymers, including surfactants, which can be completely decomposed during the carbonization step. The ease of fabrication is considered to be a major advantage when compared with other templating methods.<sup>[3]</sup> One of the typical soft-templating methods is based on using resorcinol-formaldehyde (RF) gels or similar molecular species for sol-gel processing. It is suggested that micelles formed during the process serve as templates for the generation of pores. Although wet RF particles are highly porous, upon drying the pore structure collapses and the resulting material has a relatively low surface area.<sup>[9]</sup> The issue is resolved by introducing molecular species, such as surfactants or polyelectrolytes, which after gelation can stabilize the pores during drying and carbonization. The pore structure collapse is therefore

inhibited. Despite tunable pore size through soft-templating methods, the fine-tuning of mesopore size still remains difficult because of the aggregation of the nanoparticles in the polymerizing carbon precursor matrix.<sup>[10]</sup> Additionally, the sol-gel process suffers from the drawbacks associated with the long gelation time, solvent exchange, and supercritical drying.

### **2.2.3 Ice-templating Methods**

The Giannelis group reported a novel synthetic pathway to fabricate HPCs via an ice-templating method which is a modified approach of the hard-templating technique. The HPCs synthesized via this method feature high surface areas, large pore volumes (up to 2096 m<sup>2</sup>/g and 11.4 cm<sup>3</sup>/g, respectively), and more importantly, tunable macro/meso/micro porosities.<sup>[11]</sup> Figure 2.1 shows a schematic representation of the ice-templating method. As seen from the figure, the colloidal silica nanoparticles and glucose molecules are expelled away by the growing ice crystals during the solidification of water as a result of plunging the mixture into the liquid nitrogen. The ice crystals are removed during sublimation in a freeze-dryer, generating macropores within the glucose-silica composite scaffold. The scaffold is then carbonized, resulting in a macroporous carbon-silica composite. The macropores are proved to remain intact during pyrolysis. A solution of sodium hydroxide (NaOH) is then used for etching to remove the silica nanoparticles from the composite, creating mesopores within the scaffold. Micropores are introduced by CO<sub>2</sub> activation, which further enhances the surface area, porosity, and pore volume of the material.

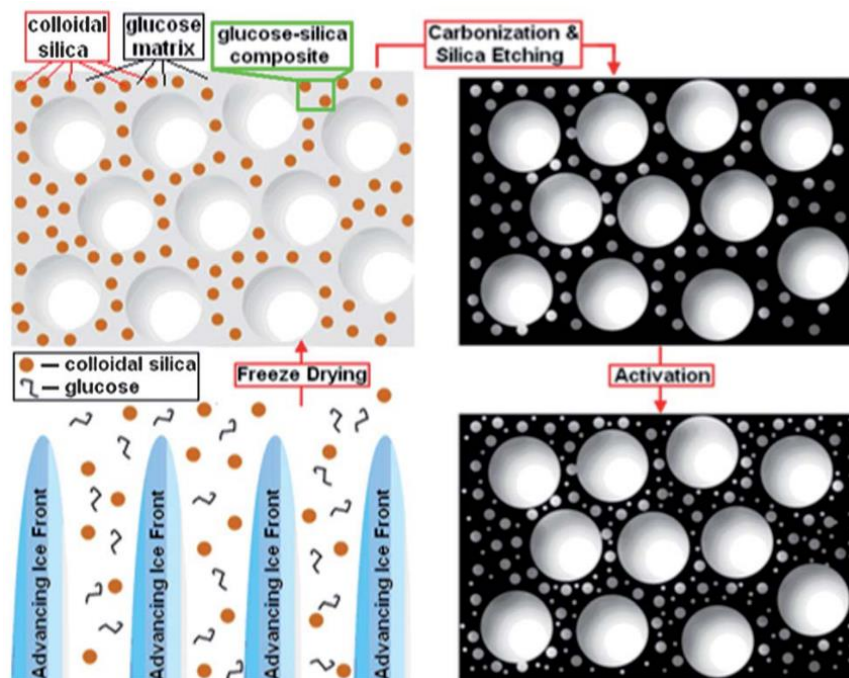


**Figure 2.1:** Schematic showing the basic steps of ice-templating method to fabricate HPCs. The four steps are shown clockwise starting from the bottom left.<sup>[11]</sup>

The macropore size and structure could be controlled by adjusting the dipping rate of the mixture into the liquid nitrogen, concentration of carbon precursor, and concentration and size of colloidal particles.<sup>[12,13]</sup> The distribution of the mesopores and the extent of mesoporosity could be simply tuned by selecting different size of silica nanoparticles or varying the silica to carbon precursor ratio. As for the microporosity, it could be controlled by changing the duration of CO<sub>2</sub> activation and the CO<sub>2</sub> gas flow rate.

For convenience, HPCs fabricated via this method are denoted by HPC- $x$ - $y$ - $z$ , where  $x$  represents the average colloidal silica nanoparticle size (nm),  $y$  represents the mass ratio of silica to glucose, and  $z$  represents the time (hours) for CO<sub>2</sub> activation.

The synthetic approach integrates ice-templating method, hard-templating method, and physical activation to fabricate HPCs featuring macro-, meso-, and microporosity in a simple material



platform. The technique provides precise control and tunability in terms of pore size and volume, especially for mesopores. The material properties of HPCs synthesized via this cost-effective ice-templating method, such as interconnected porous structure, large surface area, and high pore volume, result in the excellent performance of HPCs as electrode materials for supercapacitors and provide new opportunities for other applications including fuel cells.<sup>[11,14–16]</sup>

## **2.3 Experimental Section**

### **2.3.1 Materials**

Colloidal silica LUDOX HS-30 (12 nm, 30 wt%) and sucrose were purchased from Sigma-Aldrich. Two different nanoparticle sizes of colloidal silica (4 nm, 15 wt%) and (20 nm, 40 wt%) were purchased from Alfa Aesar Chemicals. Sodium hydroxide pellets were purchased from Macron Fine Chemicals. All chemicals were used as received without further purification.

### **2.3.2 Synthetic Procedure of HPCs with Different Mesopore Size**

HPCs with a different mesopore size were synthesized via the ice-templating approach previously reported by the Giannelis group.<sup>[11]</sup> Figure 2.2 is the schematic representation of the synthetic strategy adopted in this project of which the only difference when compared with Figure 2.1 is the carbon source utilized. First, HPCs with the mesopore size of 12 nm in diameter were synthesized. For HPC-12-1-0, 3g of sucrose (carbon source) was first added to a 50 mL centrifugation tube and dissolved in 20 mL deionized (DI) water. 10g colloidal silica suspension (12 nm, 30 wt%, Sigma-

Aldrich) was then added to the solution, and DI water was added again till the final volume of the mixture reached 40 mL HPC-4-1-0 and HPC-20-1-0 were also prepared in the similar fashion while the amount of colloidal silica solution (4 nm, 15 wt%, Alfa Aesar) and (20 nm, 40 wt%, Alfa Aesar) used was adjusted according to their weight percent in water so that silica to sucrose ratio in the mixture was 1. The centrifugation tubes were transferred to an automated shaker and mixed at 300 rpm for at least 20 mins. After the mixing process was completed, the tubes containing the precursor mixture were dipped into liquid nitrogen until solidified. The phase separation of ice crystals and solids occurred during the solidification process. The solidified precursor mixtures were freeze dried to sublime off the ice crystals for at least 2 days. Prior to the carbonization step, the monoliths after freeze-drying were ground into fine powders by a mortar. This pretreatment step was introduced to ensure thorough etching when the carbonized product was treated with NaOH solution. For the carbonization step, the powdered-like sample after grinding was transferred to a crucible made of aluminum oxide and loaded into a controlled atmosphere furnace. The mixture was calcined at 1000 °C under a constant flow of nitrogen for 3 hours at a heating rate of 5 °C/min. The mixture after the carbonization step turned into a black powder. The mixture was etched by 3M NaOH solution to remove the silica nanoparticles. For complete etching, 4.5g of the mixture after carbonization was treated with 300 mL 3M NaOH solution at 80 °C for at least 48 hours. The etching solution was then filtered and disposed. Copious amounts of DI water were used to wash off impurities till the pH value of the washings reached between 7 – 8. The final HPCs product was obtained by drying the sample in an oven at 80 °C overnight to remove any remaining water.

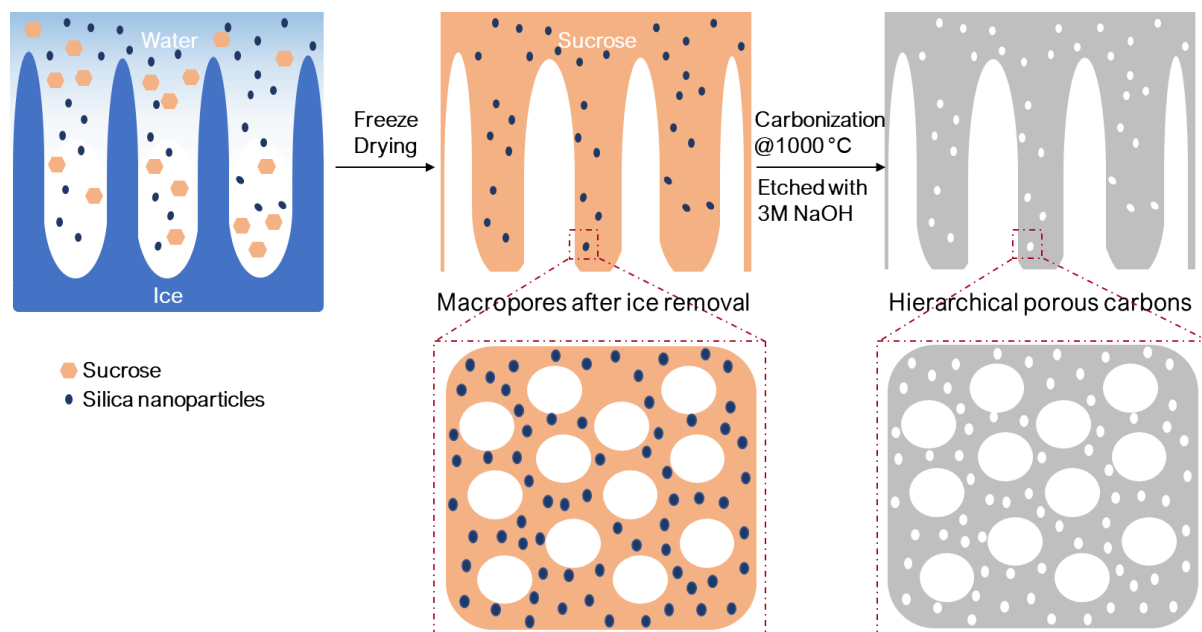


**Figure 2.2:** Schematic representation of the ice-templating combined with hard-templating method to produce HPCs.

### 2.3.3 Post Thermal Treatment for Improved Electrical Conductivity

Post thermal treatment was introduced to increase the electrical conductivity of the HPCs without altering the porosity and the structure of the materials. HPC-12-1-0 synthesized as described in section 2.3.2 was transferred to a crucible and loaded into a controlled atmosphere furnace. The sample was calcined at 900 °C under a constant flow of nitrogen for 30 mins at a heating rate of 5 °C/min. Samples after thermal treatment are referred to as HPCg-12-1-0. HPCg-4-1-0 and HPCg-20-1-0 were also synthesized following the same procedure.

## **2.4 Characterization**

The surface morphology, microstructure, and chemical composition of samples were investigated by scanning electron microscopy (SEM) and energy dispersive X-ray spectroscopy (EDS) using Zeiss Gemini 500 Scanning Electron Microscope with operating voltages between 1-5 keV. Nitrogen adsorption isotherms were recorded on Micromeritics ASAP 2460 analyzer at 77 K. The Brunauer-Emmett-Teller (BET) model was used to calculate specific surface areas of the samples. The Barrett-Joyner-Halenda (BJH) model was applied to obtain pore size distributions and total pore volumes of samples from the adsorption branch of isotherms. Raman spectra were obtained with WITec Alpha300R Confocal Raman Microscope. Elemental analysis and electronic structure were analyzed from X-ray photoelectron spectroscopy (XPS) using ESCA 2SR XPS with operating pressures of  $10^{-9}$  Torr. The samples in powder form were deposited on copper tape. Survey and high sensitivity spectra were collected at 200 eV pass energy, and high resolution at 50 eV pass energy. Electrical conductivity measurements were performed in a lab-made four-point probe setup to evaluate the electrical conductivity of samples.<sup>[16]</sup>

## **2.5 Results and Discussions**

### **2.5.1 Comparison of HPC-12-1-0 Before and After Thermal Treatment**

When compared with Vulcan XC-72 which has an electrical conductivity value of 32.71 S/cm measured by the four-point probe setup, the electrical conductivity of HPCs obtained from ice-templating method usually has a relatively low value in the order of 1 S/cm. To further improve the electrical conductivity of HPCs without altering the hierarchical porous structure, an additional

thermal treatment step was introduced. While HPC-12-1-0 has an electrical conductivity of 2.1 S/cm, the thermally treated HPCg-12-1-0 has an electrical conductivity value of 6.5 S/cm, even though according to the SEM images and AFM measurements shown in Figure 2.3 the surface morphology, mesoporosity, and roughness are similar after thermal treatment.

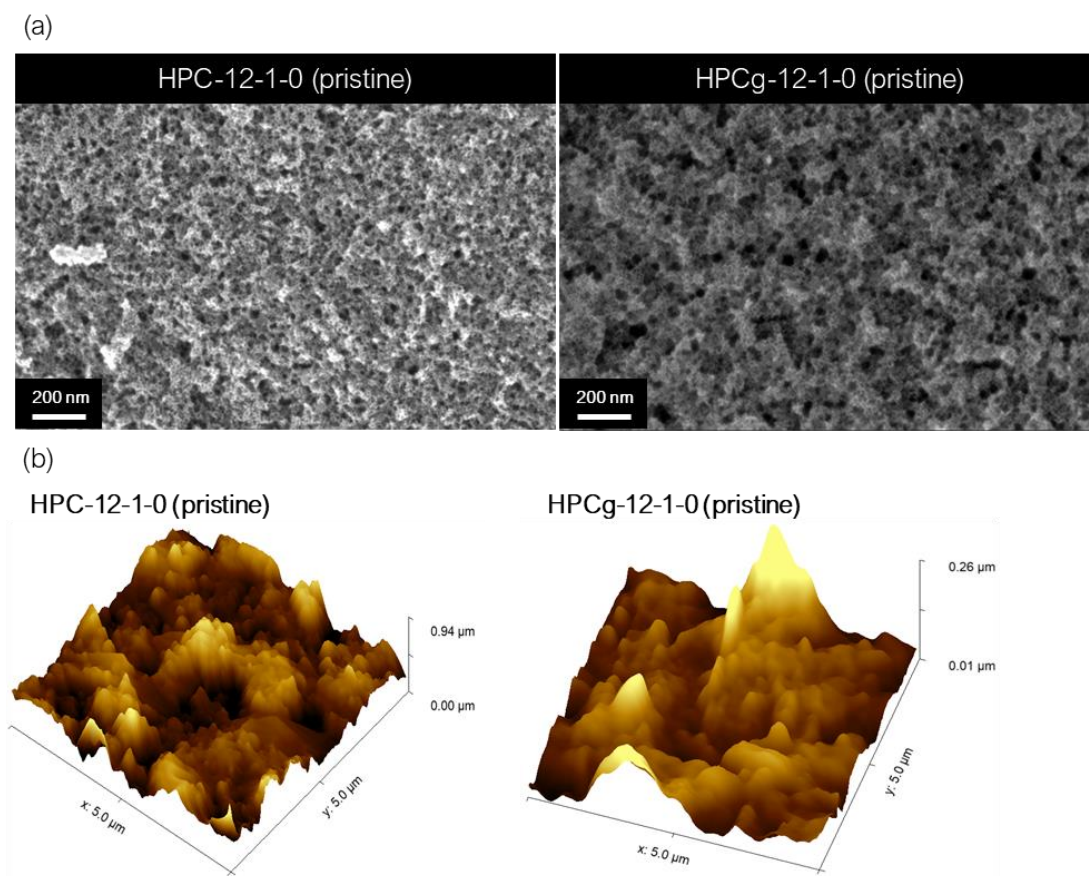


**Figure 2.3:** (a) SEM images of HPC-12-1-0 and HPCg-12-1-0 (b) AFM measurements of HPC-12-1-0 and HPCg-12-1-0.

To conduct a more quantitative analysis, nitrogen sorption and mercury porosimetry were performed to evaluate the differential pore volume of mesopores and macropores. In Figure 2.4 (a) & (b), both  $dV/dD$  pore volumes are similar before and after thermal treatment in either nitrogen

adsorption pore size distribution (PSD) or mercury PSD diagrams. Raman spectroscopy (Figure 2.4 (c)), clearly shows that the D-band/G-band ratio remains similar for the samples before and after thermal treatment. It appears that the structure of the samples remains intact after introducing the additional step of thermal treatment, and the increase of electrical conductivity is not due to any structural changes.

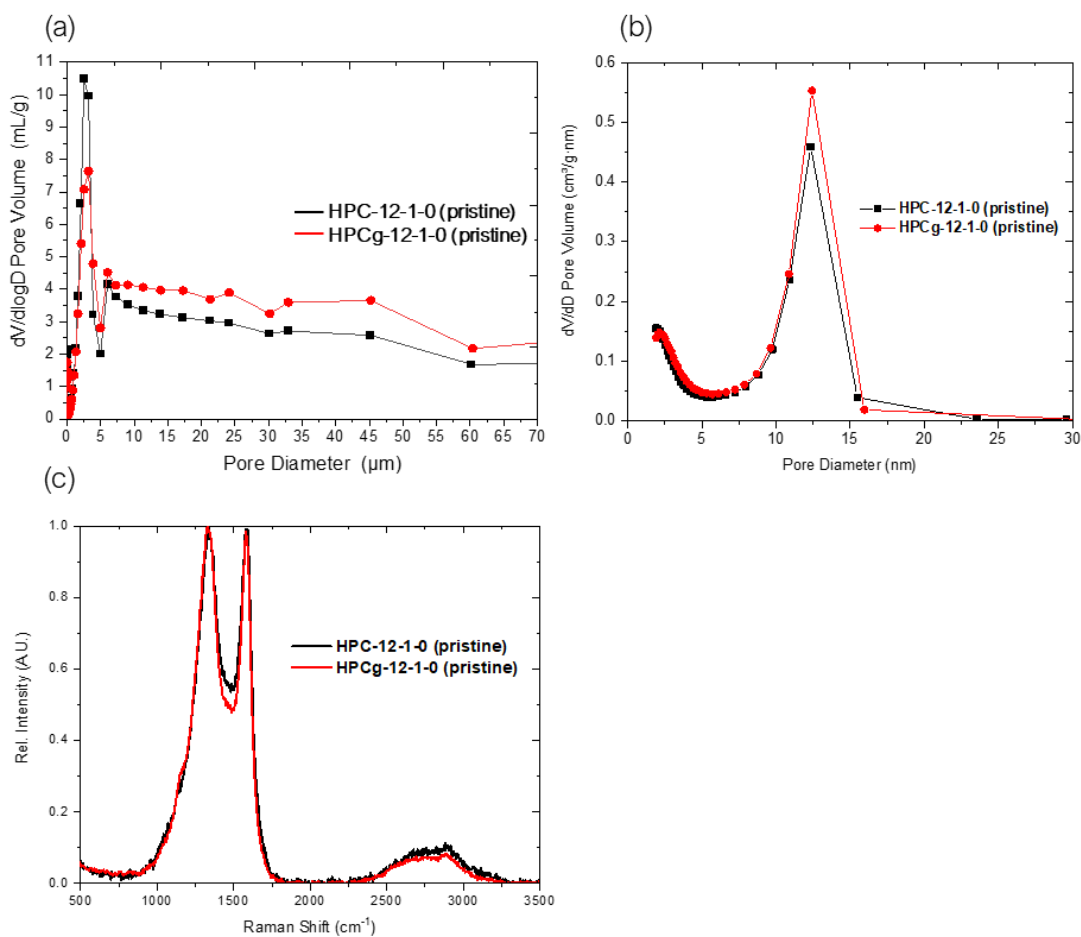


**Figure 2.4:** (a) Pore size distribution, PSD, for HPC-12-1-0 and HPCg-12-1-0 obtained by mercury porosimetry (b) PSD of HPC-12-1-0 and HPCg-12-1-0 obtained by nitrogen adsorption (c) Raman spectra of HPC-12-1-0 and HPCg-12-1-0.

EDS and XPS measurements were used to obtain chemical composition. Figure 2.5 shows the XPS spectra of HPC-12-1-0 and HPCg-12-1-0, demonstrating the survey scan for elemental analysis and high-resolution scan for chemical characterization. As seen from the survey scans in Figure 2.5 (a) & (c), HPCg-12-1-0 has lower oxygen content, when compared with HPC-12-1-0. From the high-resolution scans in Figure 2.5 (b) & (d), increased C-C/C=C ratio indicating more graphitic structure was observed in thermally treated HPCg-12-1-0.

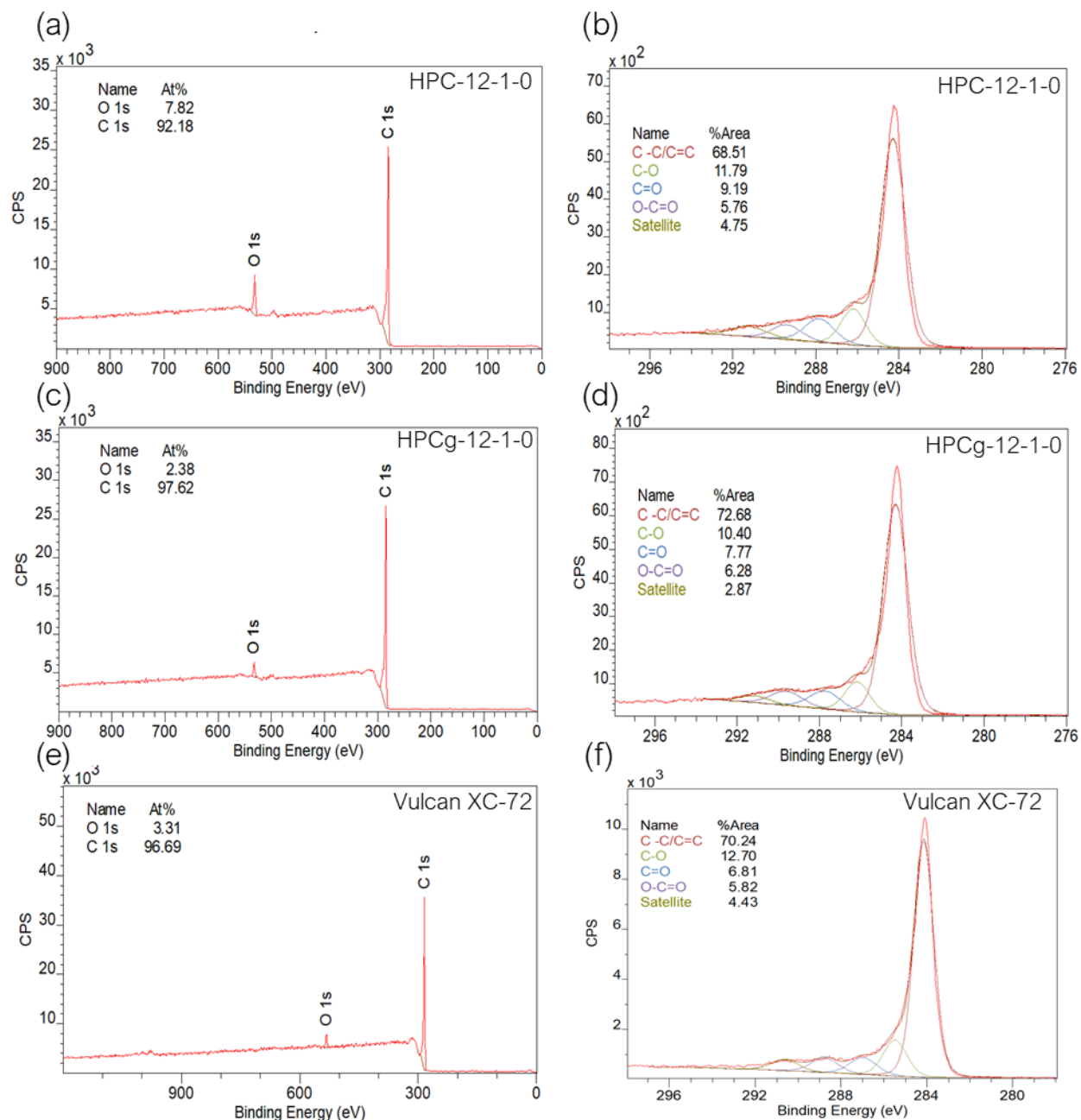


**Figure 2.5:** XPS spectra of HPC-12-1-0 and HPCg-12-1-0. Vulcan XC-72 is also included for comparison. (a) Survey scan of HPC-12-1-0 (b) high-resolution scan of HPC-12-1-0 (c) survey scan of HPCg-12-1-0 (d) high-resolution scan of HPCg-12-1-0 (e) survey scan of Vulcan XC-72 (f) high-resolution scan of Vulcan XC-72.



Since XPS focuses more on the surface composition, for complete evaluation, EDS analysis was performed to compare bulk composition (Figure 2.6). Consistent with XPS the EDS shows that HPCg-12-1-0 contains less oxygen than HPC-12-1-0. Thus the increase in electrical conductivity after thermal treatment is probably due to a decrease in oxygen content. The deoxygenation of HPCs via thermal treatment can enhance the electrical conductivity of the material without altering the porous structure.

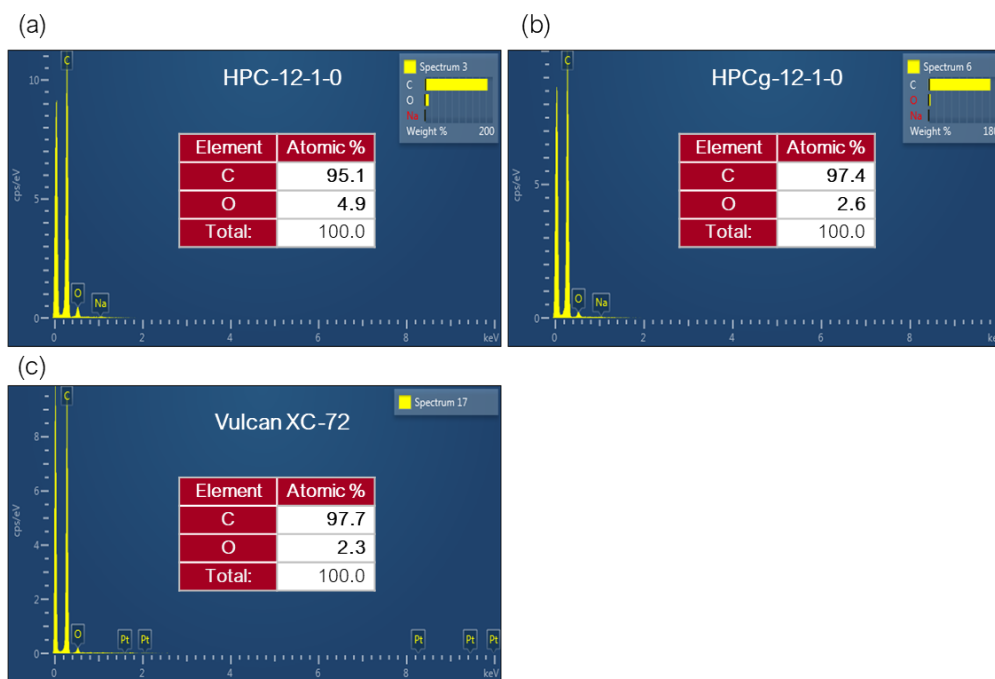


**Figure 2.6:** Energy Dispersive Spectra, EDS, and atomic percentage of HPC-12-1-0 and HPCg-12-1-0. Vulcan XC-72 is included for comparison. (a) HPC-12-1-0 (b) HPCg-12-1-0 (c) Vulcan XC-72.

### 2.5.2 Structural Investigation of HPCs with Different Mesopore Size Before and After Thermal Treatment

Table 2.1 summarizes the BET surface area, pore volume, and electrical conductivity for HPCs with different mesopore size before thermal treatment. As seen from the table, both HPC-12-1-0 and HPC-20-1-0 have similar surface area and electrical conductivity values, while HPC-4-1-0 have the highest surface area and electrical conductivity. It is believed that the smaller mesopores within the scaffold of HPC-4-1-0 result in a more interconnected network, leading to a higher electrical conductivity value.

**Table 2.1:** Surface area, pore volume, and electrical conductivity of HPCs with different mesopore size before thermal treatment.

Sample	BET surface area (m <sup>2</sup> /g)	V <sub>meso</sub> (cm <sup>3</sup> /g)	V <sub>micro</sub> (cm <sup>3</sup> /g)	Electrical conductivity (S/cm)
HPC-4-1-0	1394	2.27	0.077	5.3
HPC-12-1-0	1123	2.11	0.092	2.1
HPC-20-1-0	1112	2.21	0.112	3.4
Vulcan XC-72	210	0.40	0.032	32.7

The BET surface area, pore volume, and electrical conductivity of HPCs with different mesopore size after thermal treatment are shown in Table 2.2. From Table 2.1 and Table 2.2, it can be inferred that the surface area and pore volume remain similar before and after thermal treatment for all HPCs samples, while the electrical conductivity increases about 2 times.

**Table 2.2:** Surface area, pore volume, and electrical conductivity of HPCs with different mesopore size after thermal treatment.

<b>Sample</b>	<b>BET surface area (m<sup>2</sup>/g)</b>	<b>V<sub>meso</sub> (cm<sup>3</sup>/g)</b>	<b>V<sub>micro</sub> (cm<sup>3</sup>/g)</b>	<b>Electrical conductivity (S/cm)</b>
<b>HPCg-4-1-0</b>	1406	2.33	0.080	9.5
<b>HPCg-12-1-0</b>	1228	2.35	0.108	6.5
<b>HPCg-20-1-0</b>	1051	1.89	0.109	6.2
<b>Vulcan XC-72</b>	210	0.40	0.032	32.7

To characterize the nature of porosity due to different mesopore size and before/after thermal treatment, nitrogen adsorption-desorption isotherms and BJH PSD are presented in Figure 2.7 (a) & (b). As previously mentioned, one of the major advantages of ice-templating combined with hard-templating method, when compared with other templating techniques, is the precise control over mesopore size, which is confirmed by the PSD. All HPCs samples show a large proportion of pore size distributed around specific values, corresponding to the size of silica nanoparticle template. The high uniformity of the pore size distribution makes HPCs an ideal model system to study the pore size effect on fuel cell performance. While HPC-12-1-0, HPC-20-1-0 have highly uniform pore size distributions, HPC-4-1-0 has a slightly broader distribution with the majority still centering 4 - 5 nm. The relatively low fidelity of pore size distribution with respect to HPC-4-1-0 is also proved by the isotherm in which the hysteresis shrinks and divides into two parts, indicating non-uniform mesoporosity. SEM images (Figure 2.7 (c) – (h)) confirm that the mesopore structures are uniform for HPC-12-1-0, HPCg-12-1-0, HPC-20-1-0, and HPCg-20-1-0, whereas pore sizes vary across the surface for both HPC-4-1-0 and HPCg-4-1-0. Moreover, the mesoporosity of any HPC samples remains unchanged after thermal treatment.

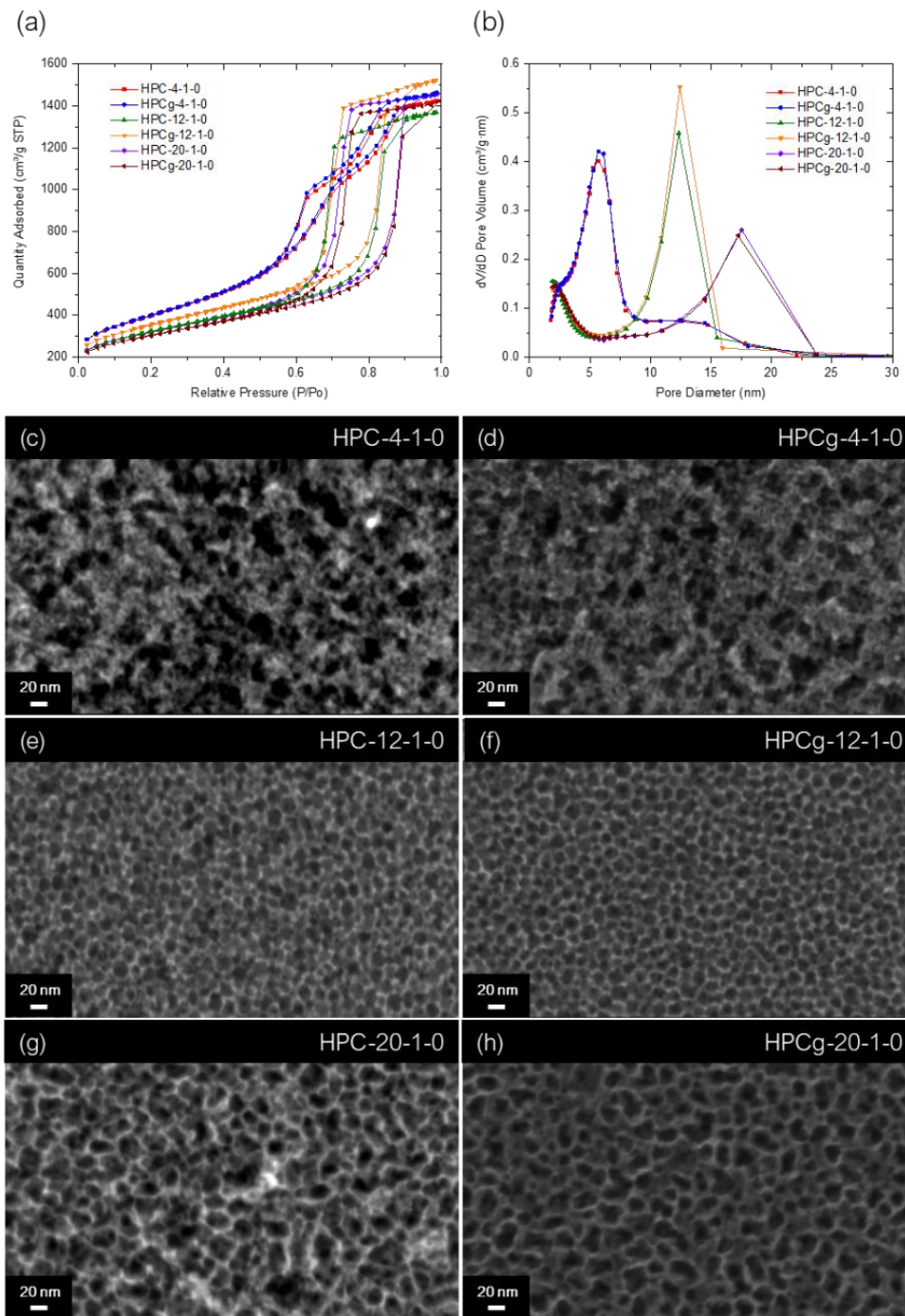


**Figure 2.7:** (a) Isotherms of HPCs with different mesopore size before and after thermal treatment (b) PSD of HPCs with different mesopore size before and after thermal treatment (c) – (h) SEM images of HPCs with different mesopore size before and after thermal treatment (c) HPC-4-1-0 (d) HPCg-4-1-0 (e) HPC-12-1-0 (f) HPCg-12-1-0 (g) HPC-20-1-0 (h) HPCg-20-1-0.

### **2.5.3 Elemental Analysis of HPCs with Different Mesopore Size**

Figure 2.8 is the EDS results of HPCs samples with different mesopore size before and after thermal treatment. Considering the difference of oxygen content between each sample before thermal treatment is less than 1 atomic percent, the chemical composition of HPCs does not vary with the size of silica nanoparticle used. In addition, all HPC samples after thermal treatment have lower oxygen content when compared with their non-thermally treated counterparts.

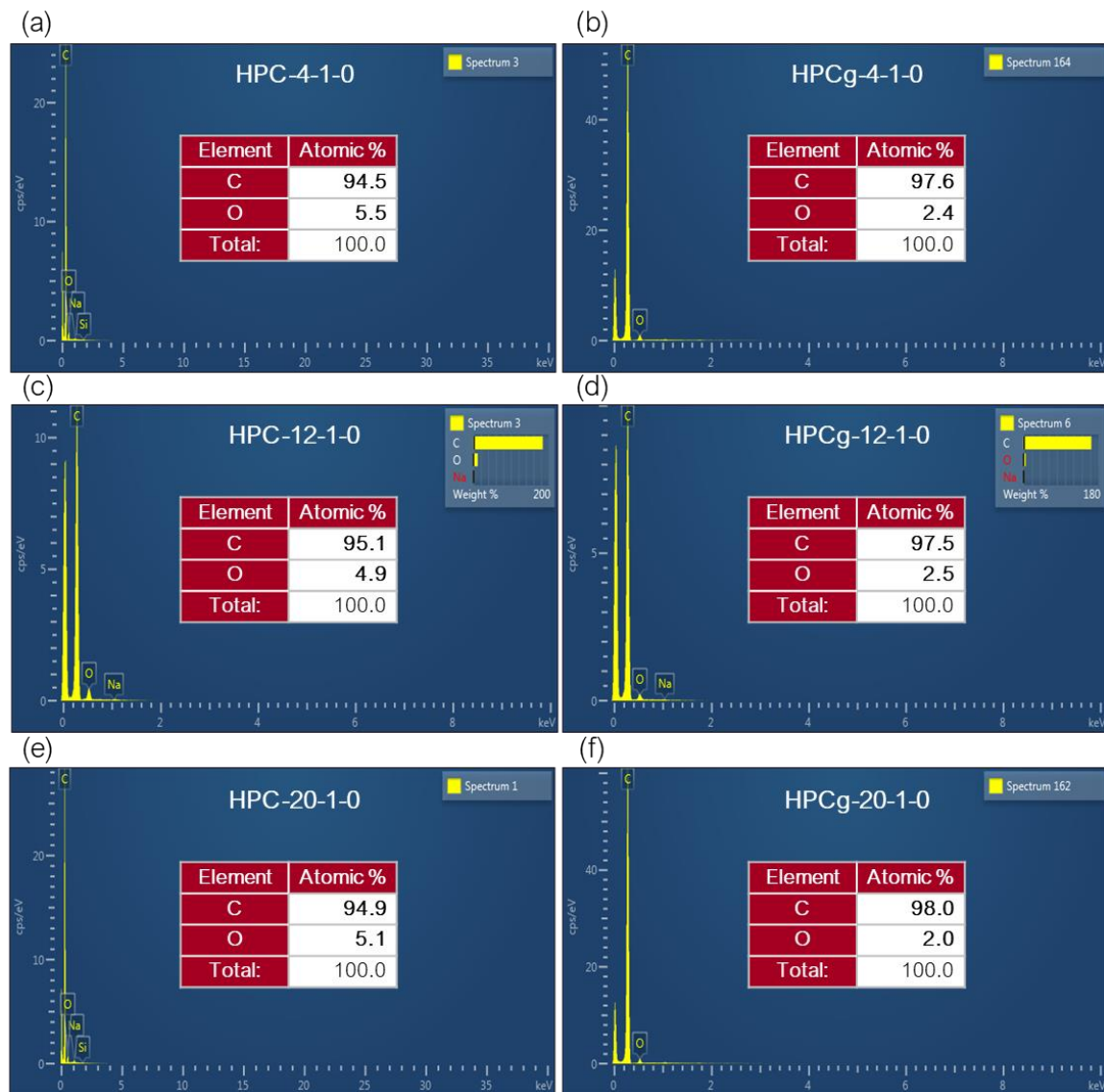


**Figure 2.8:** EDS of HPCs with different mesopore size before and after thermal treatment. (a) HPC-4-1-0 (b) HPCg-4-1-0 (c) HPC-12-1-0 (d) HPCg-12-1-0 (e) HPC-20-1-0 (f) HPCg-20-1-0.

## REFERENCES

- [1] K. S. and K. U. J. Rouquerol, D. Avnir, C. Fairbridge, D. Everett, J. Haynes, N. Pernicone, J. Ramsay, *J. Sound Vib.* **2004**, 273, 969.

- [2] W. Xin, Y. Song, *RSC Adv.* **2015**, 5, 83239.
- [3] R. W. Fu, Z. H. Li, Y. R. Liang, F. Li, F. Xu, D. C. Wu, *New Carbon Mater.* **2011**, 26, 171.
- [4] J. Pang, Q. Hu, Z. Wu, J. E. Hampsey, J. He, Y. Lu, *Microporous Mesoporous Mater.* **2004**, 74, 73.
- [5] Y. Liang, F. Liang, D. Wu, Z. Li, F. Xu, R. Fu, *Phys. Chem. Chem. Phys.* **2011**, 13, 8852.
- [6] D. W. Wang, F. Li, M. Liu, G. Q. Lu, H. M. Cheng, *Angew. Chemie - Int. Ed.* **2008**, 47, 373.
- [7] Z. Wang, F. Li, N. S. Ergang, A. Stein, *Chem. Mater.* **2006**, 18, 5543.
- [8] Z. Lei, Y. Xiao, L. Dang, S. Bai, L. An, *Microporous Mesoporous Mater.* **2008**, 109, 109.
- [9] G. Qin, W. Wei, S. Guo, *Carbon N. Y.* **2003**, 41, 851.
- [10] S. Han, T. Hyeon, *Chem. Commun.* **1999**, 1955.
- [11] L. Estevez, R. Dua, N. Bhandari, A. Ramanujapuram, P. Wang, E. P. Giannelis, *Energy Environ. Sci.* **2013**, 6, 1785.
- [12] S. Deville, C. Viazzi, C. Guizard, *Langmuir* **2012**, 28, 14892.
- [13] M. C. Gutiérrez, Z. Y. García-Carvajal, M. Jobbágy, F. Rubio, L. Yuste, F. Rojo, M. L. Ferrer, F. Del Monte, *Adv. Funct. Mater.* **2007**, 17, 3505.
- [14] R. Sahore, L. P. Estevez, A. Ramanujapuram, F. J. Disalvo, E. P. Giannelis, *J. Power Sources* **2015**, 297, 188.
- [15] L. Estevez, V. Prabhakaran, A. L. Garcia, Y. Shin, J. Tao, A. M. Schwarz, J. Darsell, P.

Bhattacharya, V. Shutthanandan, J. G. Zhang, *ACS Nano* **2017**, *11*, 11047.

- [16] R. Sahore, B. D. A. Levin, M. Pan, D. A. Muller, F. J. DiSalvo, E. P. Giannelis, *Adv. Energy Mater.* **2016**, *6*, 1.



## CHAPTER 3

# **BALANCING SURFACE AREA AND ELECTRICAL CONDUCTIVITY OF HIERARCHICAL POROUS CARBONS – GRAPHENE NANOPATELETS COMPOSITES AS NOVEL FUEL CELL CATALYST SUPPORTS**

### **3.1 Introduction**

As mentioned in Section 2.5.1, one of the main deficits concerning HPCs as fuel cell catalyst supports when compared with other common carbon supports is the relatively low electrical conductivity ( $\sim 1$  S/cm). Electrical conductivity of carbon materials is highly related to the electronic structure. Common carbon catalyst supports, especially CNTs, exhibit high electrical conductivity owing to their graphite-like structure and high aspect ratio. Only graphene with a layer morphology has obtained electrical percolation thresholds comparable to CNTs and excellent electronic properties.<sup>[1]</sup> To give a general idea, electrical conductivities as high as  $2 \times 10^5$  and  $2 \times 10^3$  S/cm respectively for SWCNT and MWCNT were measured.<sup>[2,3]</sup> Graphite with electrical conductivities around  $10^3$ - $10^4$  and  $10$ - $10^2$  S/cm in parallel and perpendicular directions to the graphene layers, respectively has also been reported by Charlier et al.<sup>[4]</sup> On the other hand, the bulk electrical conductivity (or powder electrical conductivity) of carbon materials depends not only on the electronic structure but also particle shape and their degree of compaction. Under pressure, the higher the number of contacts among particles, the higher the number of conduits available for transport of electric current.<sup>[5]</sup> Marinho et al. reported the powder electrical conductivity and isolated single particle electrical conductivity of MWCNTs, graphene, carbon black, and graphite, which are summarized in Table 3.1.<sup>[6]</sup>

**Table 3.1:** Materials and compact characteristics.<sup>[6]</sup>

Filler	BET surface area (m <sup>2</sup> /g)	Conductivity (S/m)			
		Powder compact at 5 MPa	Paper	Isolated Single particle conductivity	Filler contribution limit from compact <sup>a</sup>
MWCNTs	272	$5.43 \times 10^2$	$5 \times 10^3$	$10^6$ – $10^7$ <sup>b</sup>	$10.3 \times 10^3$
Graphene	180	$2.62 \times 10^2$	$1.4 \times 10^3$	$10^7$ – $10^8$ [2]	$10.9 \times 10^3$
Carbon Black	56.9	$5.58 \times 10^2$	$9 \times 10^1$	$10^3$ [14]	$8.8 \times 10^3$
Graphite	3.08	$2.12 \times 10^3$	$1.2 \times 10^3$	$10^5$ [27] <sup>c</sup>	$13.8 \times 10^3$

<sup>a</sup> Estimate based on the model as described in [17].

<sup>b</sup> As provided by the Nanocyl Company: <http://www.nanocyl.com/en/CNT-Expertise-Centre/Carbon-Nanotubes>.

<sup>c</sup> Value highly variable depending on source.

In addition to the aspect ratio or the particle shape, other parameters including surface area, porosity, anisotropy, impurity content or surface functionalization also play significant roles in affecting the electrical conductivity of the carbon catalyst supports.<sup>[1]</sup> It is known in carbon materials that the porosity can sensitively influence the electrical conductivity, and in effect electrical conductivity usually decreases with increasing porosity.<sup>[7]</sup> Moreover, despite impeding electronic conduction in the carbon network, oxygen functionalization is a useful technique to improve the homogeneity and interfacial bonding between carbon catalyst supports and electrocatalysts with surface oxygen acting as anchoring sites. Conversely, electrical conductivity of carbon materials can be enhanced by deoxygenation. The effect of surface chemistry on electrical conductivity among different carbon materials has been investigated and reported by various research groups.<sup>[8–10]</sup> In this chapter, the goal is to improve the electrical conductivity of HPCs by creating novel composite catalyst supports comprising HPCs and highly conductive carbon additives, such as CNT and graphene nanoplatelets (GN).

## **3.2 Experimental Section**

### **3.2.1 Materials**

Colloidal silica LUDOX HS-30 (12 nm, 30 wt%), sucrose, graphene nanoplatelets (surface area: 300 m<sup>2</sup>/g), multi-walled carbon nanotubes, and oxidized multi-walled carbon nanotubes were purchased from Sigma-Aldrich. Sodium hydroxide pellets were purchased from Macron Fine Chemicals. All chemicals were used as received without further purification.

### **3.2.2 Synthetic Procedure of HPCs-GN Composites**

HPCs-GN composites were fabricated via a modified ice-templating approach previously reported by the Giannelis group.<sup>[11]</sup> 3g of sucrose (carbon source) was first mixed with 10 mL colloidal silica suspension (12 nm, 30 wt%, Sigma-Aldrich) and 30 mL DI water in a 50 mL centrifugation tube. Several tubes were prepared following the previous step, and graphene nanoplatelets were added proportionally to the sample-containing tubes so the final weight ratios of GN to sucrose were: 0:1 (pristine), 2:15 (12% GN), 1:3 (25% GN), 2:3 (40% GN), and 1:1 (50% GN). Another sample containing only GN (GN to sucrose ratio: 1:0, namely 100% GN) was also prepared for comparison. The mixtures were then sonicated for 5 mins to facilitate GN suspension. An automated shaker was then used to attain thorough mixing at 300 rpm for at least 20 mins. After the mixing process was completed, they were then dipped in liquid nitrogen until solidified. Freeze drying was used to remove ice crystals via sublimation for at least 2 days. Before performing carbonization, the composite materials after freeze-drying were ground into fine powders by a

mortar. This pretreatment step was introduced to ensure thorough etching when the carbonized product was treated with NaOH solution. With increasing amount of GN incorporated, the HPCs-GN composites could be more easily ground, generating finer particles. For the carbonization step, the powdered-like composite materials after grinding were transferred to a crucible and loaded into a controlled atmosphere furnace. The mixture was calcined at 1000 °C under a constant flow of nitrogen for 3 hours at a heating rate of 5 °C/min. The mixture after the carbonization step turned into a black powder. To completely remove silica nanoparticles via etching, 4.5g black powdered mixture was dispersed and vigorously stirred in 300 mL 3M sodium hydroxide (NaOH) solution at 80 °C for at least 48 hours. The etching solution was then filtered and disposed. Copious amounts of DI water were then used to wash off the impurities till the pH value of the washings reached between 7 - 8. The final HPCs-GN composites were obtained by drying the samples in an oven at 80 °C overnight to remove any remaining water.

### **3.2.3 Post Thermal Treatment for Improved Electrical Conductivity**

Post thermal treatment was introduced to increase the electrical conductivity of the HPCs-GN composite without altering the porosity and the structure of the materials. The HPCs-GN composite obtained from Section 3.2.2 was transferred to a crucible and loaded into a controlled atmosphere furnace. The composite was calcined at 900 °C under a constant flow of nitrogen for 30 mins at a heating rate of 5 °C/min.

## **3.4 Results and Discussions**

### **3.3 Characterization**

The surface morphology, microstructure, and chemical composition of samples were investigated by scanning electron microscopy (SEM) and energy dispersive X-ray spectroscopy (EDS) using Zeiss Gemini 500 Scanning Electron Microscope with operating voltages between 1-5 keV. Nitrogen adsorption isotherms were recorded on Micromeritics ASAP 2460 analyzer at 77 K. The Brunauer-Emmett-Teller (BET) model was used to calculate specific surface areas of the samples. The Barrett-Joyner-Halenda (BJH) model was applied to obtain pore size distributions and total pore volumes of samples from the adsorption branch of isotherms. Elemental composition and electronic structure were analyzed from X-ray photoelectron spectroscopy (XPS) using ESCA 2SR XPS with operating pressures of  $10^{-9}$  Torr. The samples in powder form were deposited on copper tape. Survey and high sensitivity spectra were collected at 200 eV pass energy, and high resolution at 50 eV pass energy. Electrical conductivity measurements were performed in a lab-made four-point probe setup to evaluate the electrical conductivity of samples.<sup>[12]</sup>

#### **3.4.1 Comparison between Composite HPCs with Different Carbon Additives**

As mentioned in Section 1.1.2, the concept of combining two carbon supports as a novel catalyst support has been adopted by several research groups. When compared to other common carbon supports used in fuel cells such as carbon black, graphene, and carbon nanotubes, one of HPCs main deficits is its relatively low electrical conductivity. In this chapter, to optimize HPCs as fuel

cell catalyst supports, I focused on increasing the overall electrical conductivity by incorporating another carbon support featuring higher electrical conductivity. First, graphene nanoplatelets (GN) and multi-walled carbon nanotubes (MWCNT) were utilized as different additives for comparison due to their outstanding electrical conductivities. The synthetic strategy adopted in this work is demonstrated in Figure 3.1. It is a modified synthetic pathway based on the ice-templating method previously reported by the Giannelis group, through which composite HPCs materials such as HPCs-GN and HPCs-MWCNT were generated.<sup>[11]</sup> Nevertheless, one of the main issues concerning MWCNT as additives in this system is their low dispersity in water even after sonication, which hinders uniform distribution of MWCNT materials in the HPCs. To address this problem, oxidized MWCNT (ox-MWCNT) were used as the other additives with the hope of enhancing the material dispersion in water owing to their improved hydrophilicity.

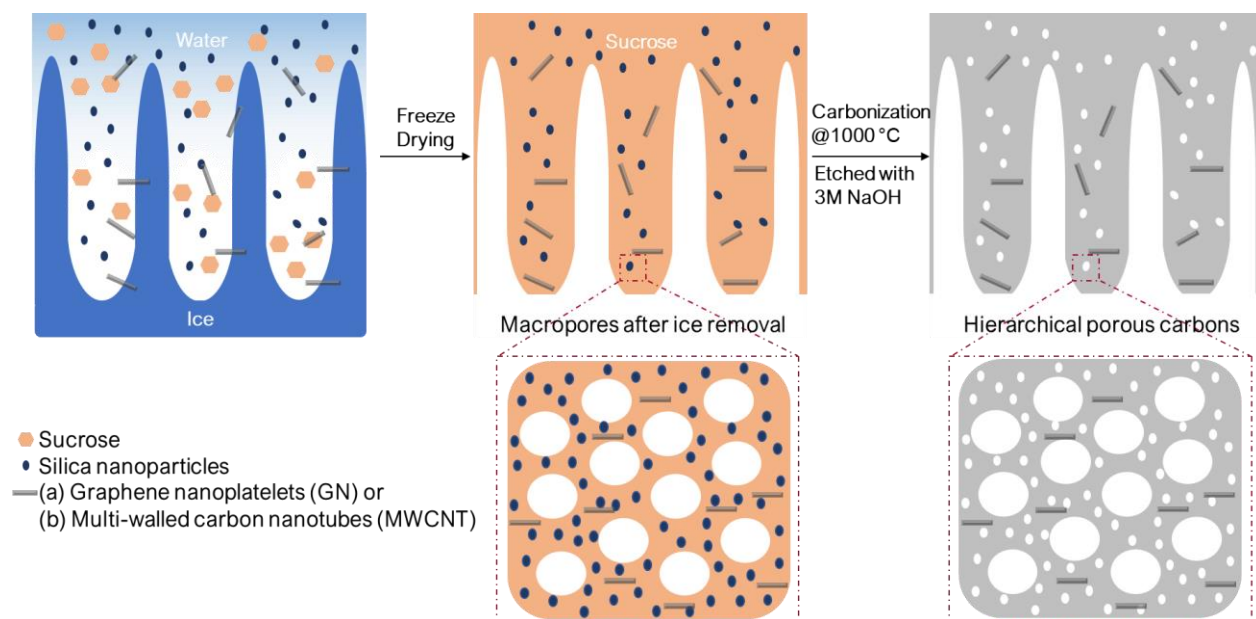


**Figure 3.1:** Schematic representation of the ice-templating combined with hard-templating method to produce HPCs-GN or HPCs-MWCNT composites.

Figure 3.2 shows the SEM images of the resulting three different HPCs composites with the identical weight mass of additives. HPCs-GN, HPCs-MWCNT, and HPCs-ox-MWCNT refer to samples containing graphene nanoplatelets, multi-walled carbon nanotubes, and oxidized multi-walled carbon nanotubes, respectively. As seen from the images in Figure 3.2 (a), (c), and (e) taken at lower magnification, the distribution of additives were worse for HPCs-MWCNT with MWCNT forming bulky aggregates. ox-MWCNT has the best dispersion while GN is in between. At higher magnification shown in Figure 3.2 (b), (d), and (f), the anchoring of materials on the HPCs was clearly seen for all additives, which validates the feasibility of incorporating different carbon materials into HPCs to create novel composite supports.

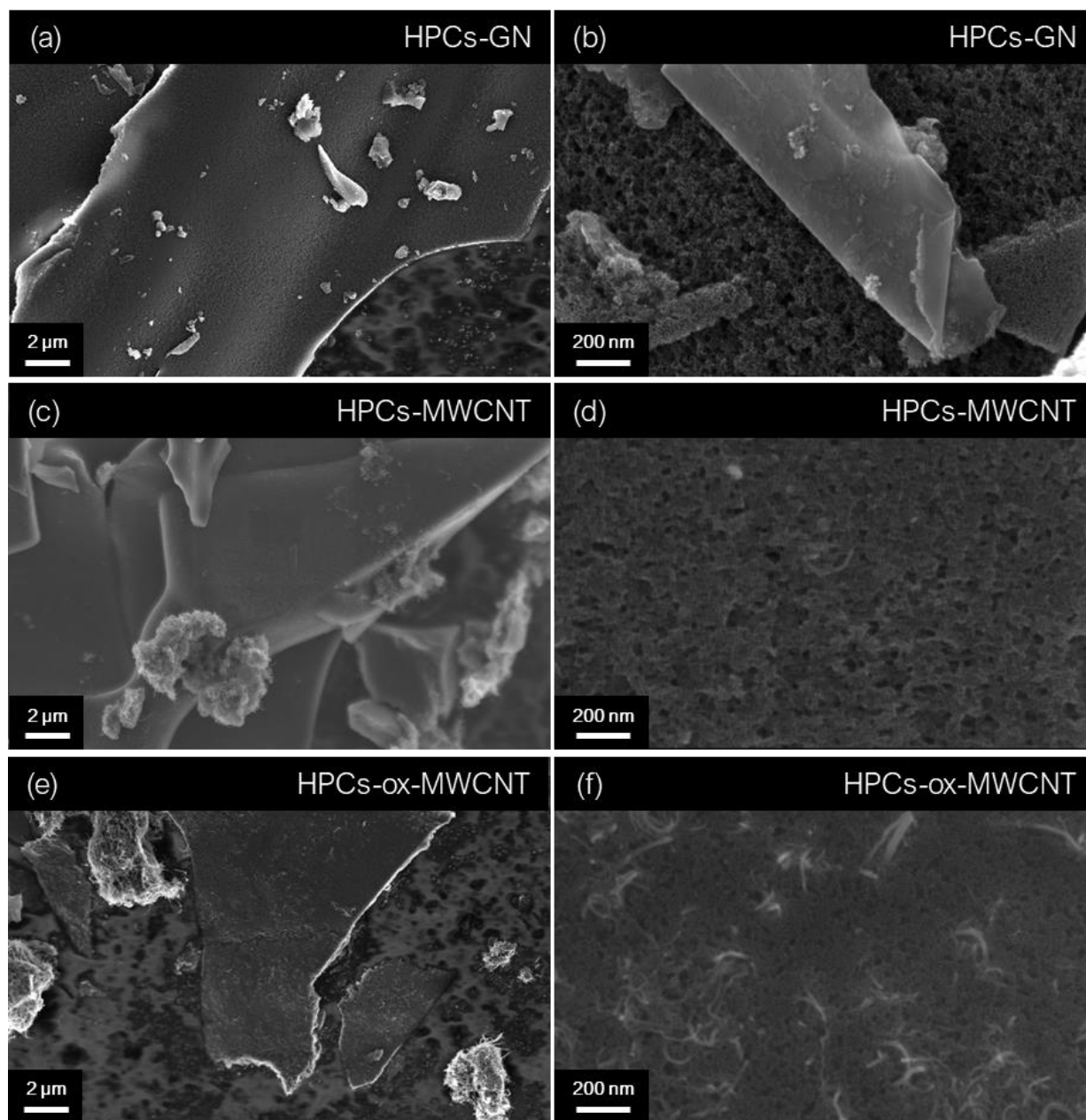


**Figure 3.2:** SEM images of different HPCs composites at low and high magnification. (a,b) HPCs-GN (c,d) HPCs-MWCNT (e,f) HPCs-ox-MWCNT.

The three composite materials were further compared by evaluating their BET surface area and electrical conductivity, and the results are summarized in Table 3.2. It turned out that the relatively



cost-effective carbon additive (which was GN in this case) improved the electrical conductivity of the composite significantly while slightly decreasing the surface area.

**Table 3.2:** Surface area, pore volume, and electrical conductivity of composite HPCs with different carbon additives. Vulcan XC-72 is included for comparison.

<b>Sample</b>	<b>BET surface area (m<sup>2</sup>/g)</b>	<b>V<sub>meso</sub> (cm<sup>3</sup>/g)</b>	<b>V<sub>micro</sub> (cm<sup>3</sup>/g)</b>	<b>Electrical conductivity (S/cm)</b>
<b>HPCs-GN</b>	714	1.36	0.057	8.5
<b>HPCs-MWCNT</b>	571	1.44	0.045	6.9
<b>HPCs-ox-MWCNT</b>	645	1.60	0.042	5.1
<b>Vulcan XC-72</b>	210	0.40	0.032	32.7

### 3.4.2 Structural Analysis of HPCs-GN Composites

From the previous section, it can be inferred that the specific surface area of the composite decreases with increasing content of carbon additives whereas the electrical conductivity increases. A thorough study of HPCs-GN composite was conducted and the results of surface area and electrical conductivity are shown in Figure 3.3. A sample made with GN only (without any sucrose) was also fabricated for comparison. The specific surface area decreases proportionally to the amount of GN incorporated but the increase of electrical conductivity does not. At 50 wt% (GN to sucrose weight ratio = 1:1) GN content, the HPC structure can no longer be generated, meaning silica nanoparticles cannot serve as an effective hard template, when the amount of carbon additives is above 50 wt%.

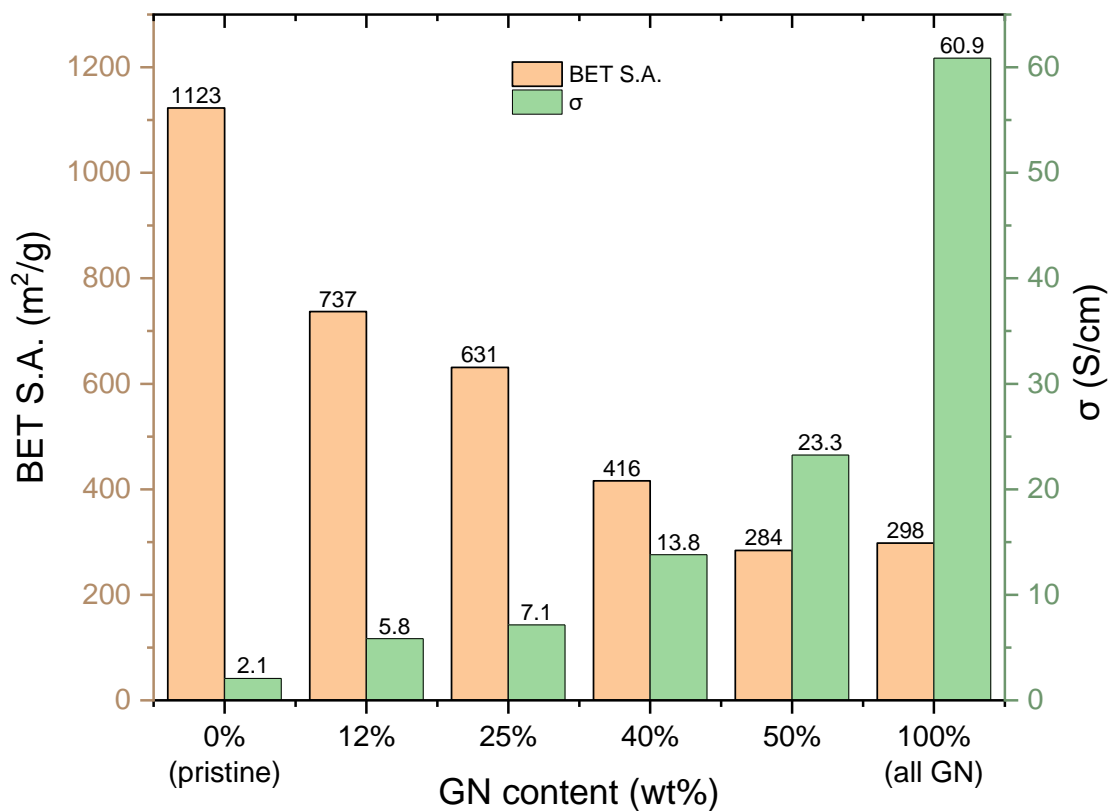


**Figure 3.3:** Surface area and electrical conductivity of HPCs-GN containing various amounts of GN.

The  $N_2$  adsorption isotherms of the HPCs-GN composites are provided in Figure 3.4 (a). The extent of mesoporosity is reduced with increasing GN content, which is confirmed from the shrinkage of hysteresis. Pore size distributions (PSD) of HPCs-GN composites are shown in Figure 3.4 (b). The majority of mesopores centers at 12 nm, corresponding to the size of silica nanoparticle used during synthesis. However, from the PSD diagrams the relative volume of mesopores decreases with increasing GN content.

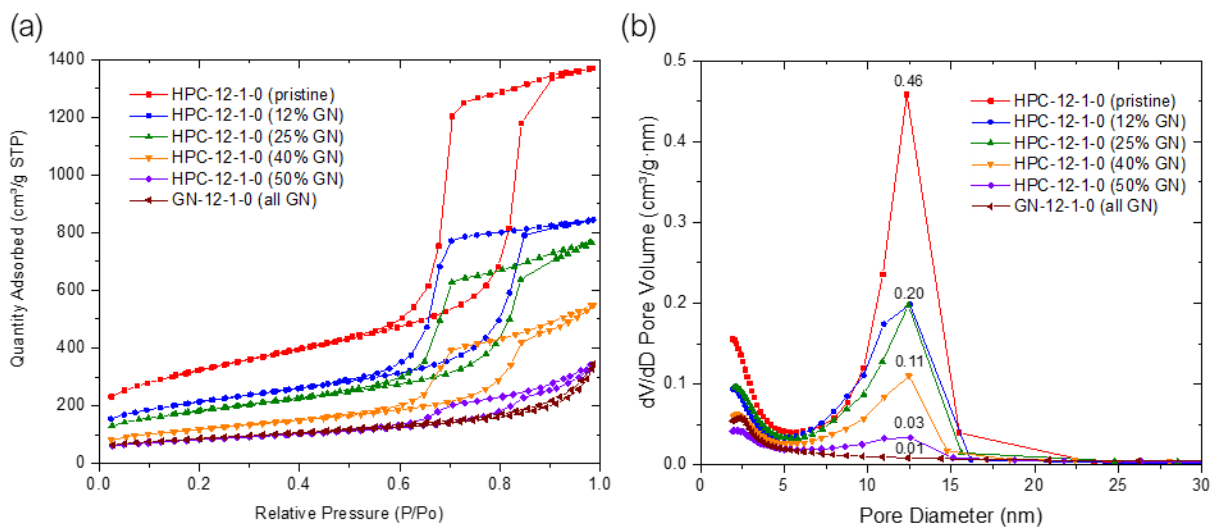


**Figure 3.4:** (a) Isotherms and (b) pore size distributions, PSD, of HPCs-GN composites with various amounts of GN.

All of the composites in Figure 3.3 have relatively low electrical conductivities. To further improve the electrical conductivity of the composite without altering the hierarchical porous structure, an additional step of thermal treatment was again introduced. The electrical conductivity and BET surface area values after the step of thermal treatment are shown in Figure 3.5. The samples after thermal treatment are denoted as HPCg for convenience. With properly controlled thermal treatment, the electrical conductivity of the composites increases about 2 times while the surface area is retained.

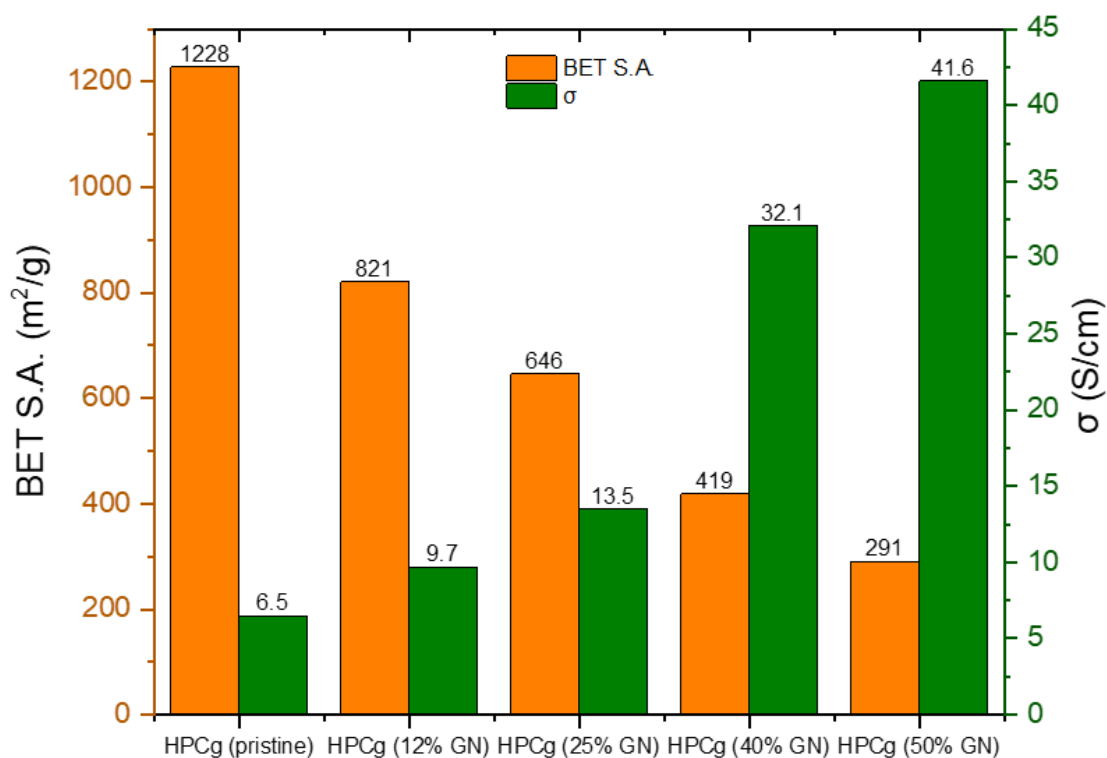


**Figure 3.5:** Surface area and electrical conductivity of HPCs-GN containing different amounts of GN after the step of thermal treatment.

It is also confirmed from nitrogen adsorption isotherms and PSD diagrams shown in Figure 3.6 that the mesoporosity and mesoporous structure remain unchanged for all HPC composites after the additional thermal treatment.

It is important to mention that HPCg-12-1-0 (40% GN) now has a surface area value 2 times higher than that of Vulcan XC-72 with comparable electrical conductivity.

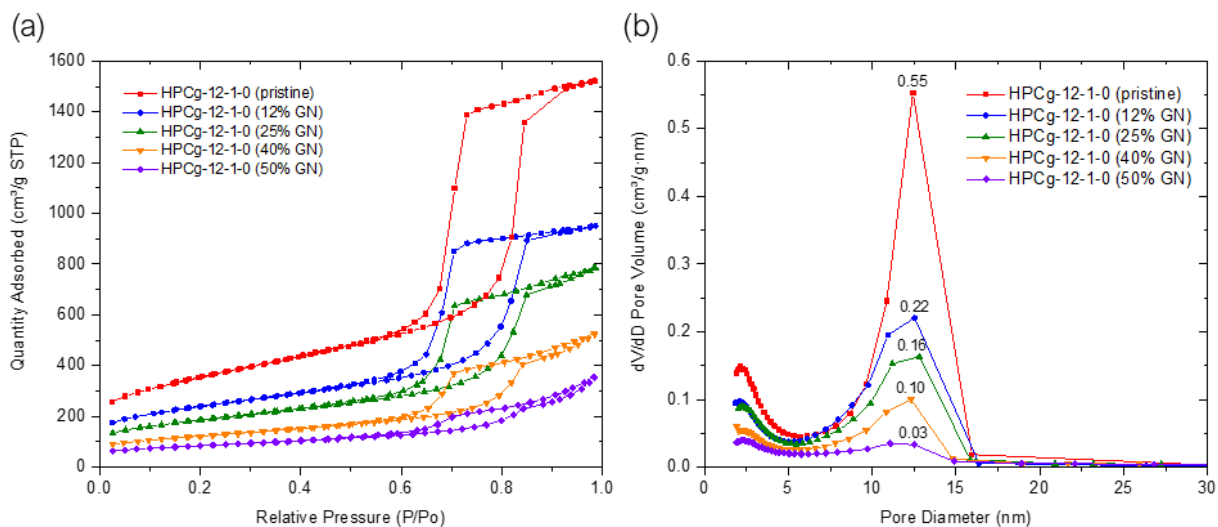


**Figure 3.6:** (a) Isotherms of thermally-treated HPCs-GN composites containing different amounts of GN (b) PSD.

As shown in Table 3.3, the total pore volume including both mesopores and micropores, decreases with increasing content of graphene nanoplatelets, and again at 50 wt% GN, a hierarchical structure can no longer be generated.

**Table 3.3:** Pore volume of composite HPCs with different amounts of GN before and after thermal treatment. Vulcan XC-72 and a sample of pure GN are included for comparison.

Sample	$V_{\text{meso}}$ ( $\text{cm}^3/\text{g}$ )	$V_{\text{micro}}$ ( $\text{cm}^3/\text{g}$ )	Sample	$V_{\text{meso}}$ ( $\text{cm}^3/\text{g}$ )	$V_{\text{micro}}$ ( $\text{cm}^3/\text{g}$ )
HPC-12-1-0 (pristine)	2.11	0.092	HPCg-12-1-0 (pristine)	2.35	0.108
HPC-12-1-0 (12% GN)	1.29	0.070	HPCg-12-1-0 (12% GN)	1.46	0.081
HPC-12-1-0 (25% GN)	1.22	0.045	HPCg-12-1-0 (25% GN)	1.25	0.052
HPC-12-1-0 (40% GN)	0.87	0.016	HPCg-12-1-0 (40% GN)	0.81	0.034
HPC-12-1-0 (50% GN)	0.51	0.025	HPCg-12-1-0 (50% GN)	0.53	0.030
Graphene nanoplatelet	0.47	0.032	Vulcan XC-72	0.40	0.032

### 3.4.3 Compositional Analysis of HPCs-GN Composites

To evaluate the effect of carbon additives on composition of HPCs-GN composites, XPS and EDS measurements were performed. HPC-12-1-0 (pristine) and HPC-12-1-0 (40% GN) before and after thermal treatment were selected for comparison, since they show different electrical conductivity and surface area values. Figure 3.7 shows the XPS spectra of survey and high-resolution scans of HPC-12-1-0 (pristine) and HPC-12-1-0 (40% GN) before thermal treatment. Incorporation of graphene nanoplatelets slightly lowers the oxygen content of the composites, whereas the chemical bonding remains similar for both samples according to high-resolution scans. Still, both HPC-12-1-0 (pristine) and HPC-12-1-0 (40% GN) have higher oxygen content compared to the commercial Vulcan XC-72.

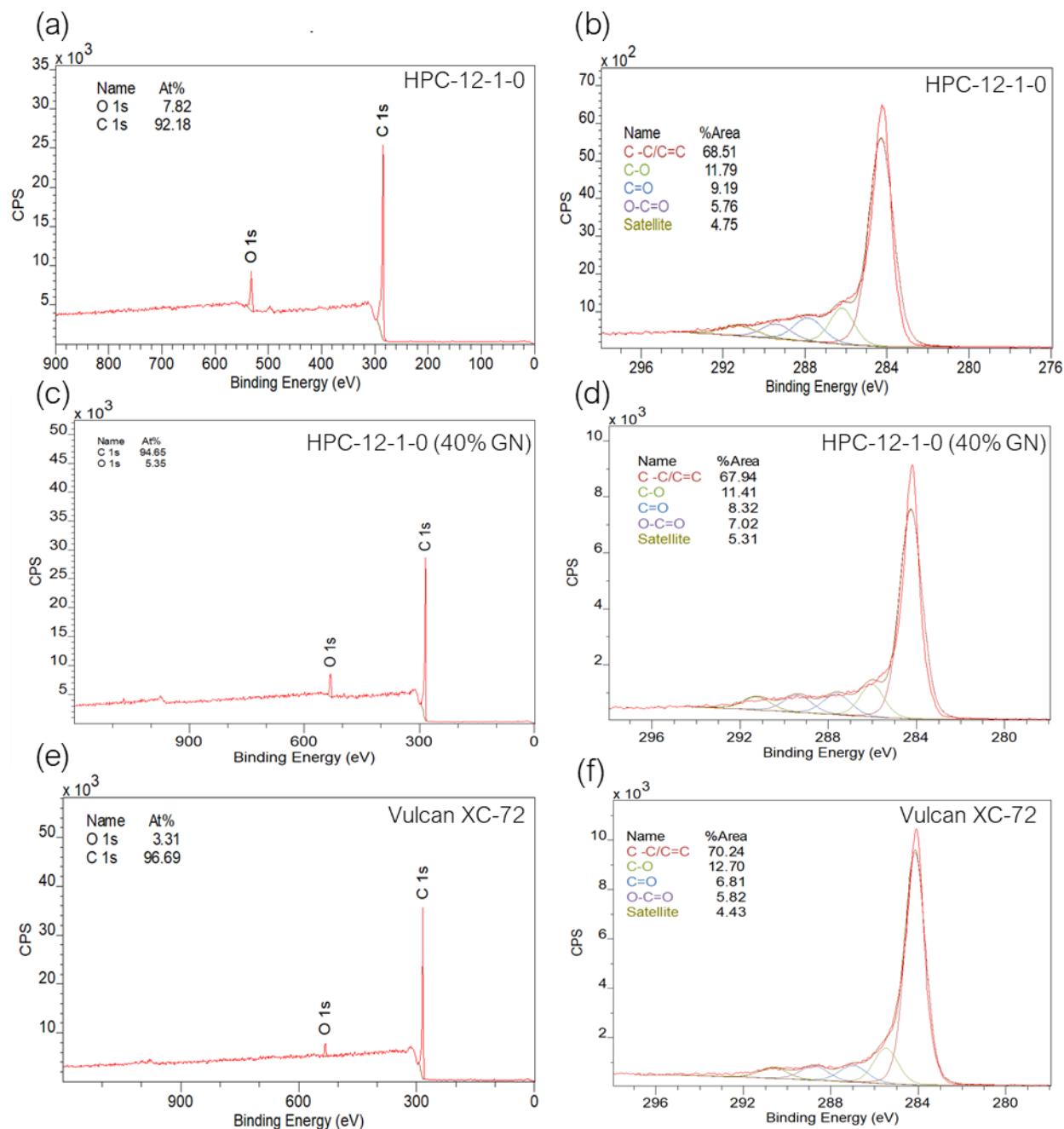


**Figure 3.7:** XPS spectra of HPC-12-1-0 (pristine) and HPC-12-1-0 (40% GN). Vulcan XC-72 is included for comparison. (a) Survey scan of HPC-12-1-0 (pristine) (b) high-resolution scan of HPC-12-1-0 (pristine) (c) survey scan of HPC-12-1-0 (40% GN) (d) high-resolution scan of HPC-12-1-0 (40% GN) (e) survey scan of Vulcan XC-72 (f) high-resolution scan of Vulcan XC-72.

Figure 3.8 shows the XPS spectra of survey and high-resolution scans of HPC-12-1-0 (pristine) and HPC-12-1-0 (40% GN) after thermal treatment. Recall that for the thermally-treated samples, the oxygen content decreases (e.g. HPCg-12-1-0 (pristine)), as discussed in Section 2.5.1. The increase of electrical conductivity for both pristine HPC and composite HPCs-GN is probably due to deoxygenation.



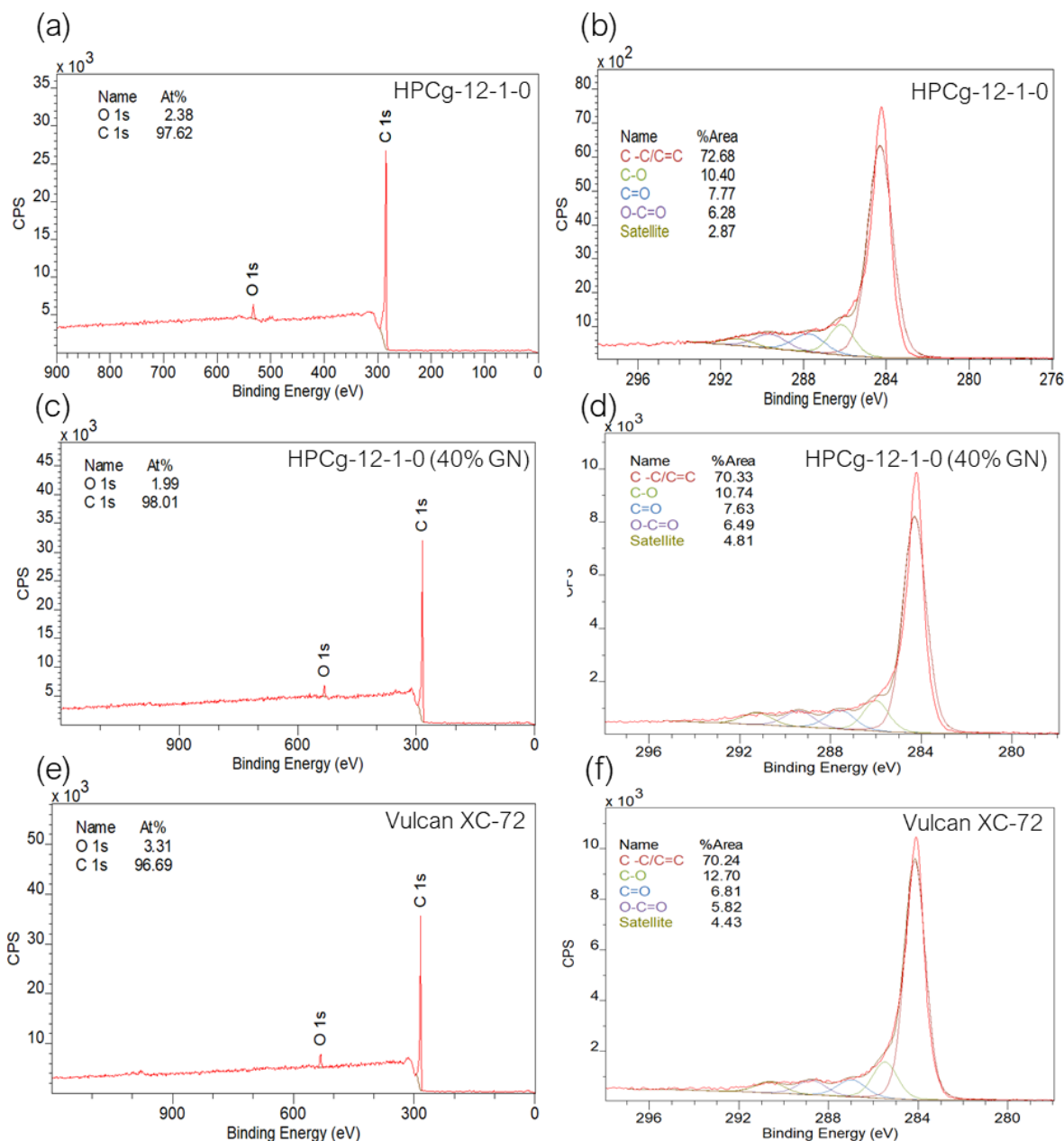


**Figure 3.8:** XPS spectrum of thermally treated HPC-12-1-0 (pristine) and HPC-12-1-0 (40% GN). Vulcan XC-72 is included for comparison. (a) Survey scan of HPCg-12-1-0 (pristine) (b) high-resolution scan of HPCg-12-1-0 (pristine) (c) survey scan of HPCg-12-1-0 (40% GN) (d) high-resolution scan of HPCg-12-1-0 (40% GN) (e) survey scan of Vulcan XC-72 (f) high-resolution scan of Vulcan XC-72.

In addition to XPS measurements, EDS results of HPC-12-1-0 (pristine) and HPC-12-1-0 (40% GN) before and after thermal treatment are presented in Figure 3.9. EDS confirms that deoxygenation does occur in the bulk (not just the surface probed by XPS), indicating uniform oxygen content reduction for both samples after thermal treatment. Both HPCg-12-1-0 (pristine) and HPCg-12-1-0 (40% GN) have similar elemental composition to commercial product Vulcan XC-72.

To sum up, HPCg-12-1-0 (40% GN) shows a surface area 2 times higher than Vulcan XC-72 with comparable electrical conductivity. The micropore volume for both samples are similar, while the mesopore volume for the HPCg-12-1-0 (40% GN) is double. Moreover, the elemental composition of the surface and interior are also similar for HPCg-12-1-0 (40% GN) and Vulcan XC-72. In the following I used HPCg-12-1-0 (pristine) and HPCg-12-1-0 (40% GN) for electrocatalyst deposition, and compare them with the commercial standard Pt/Vulcan XC-72 in Chapter 4.

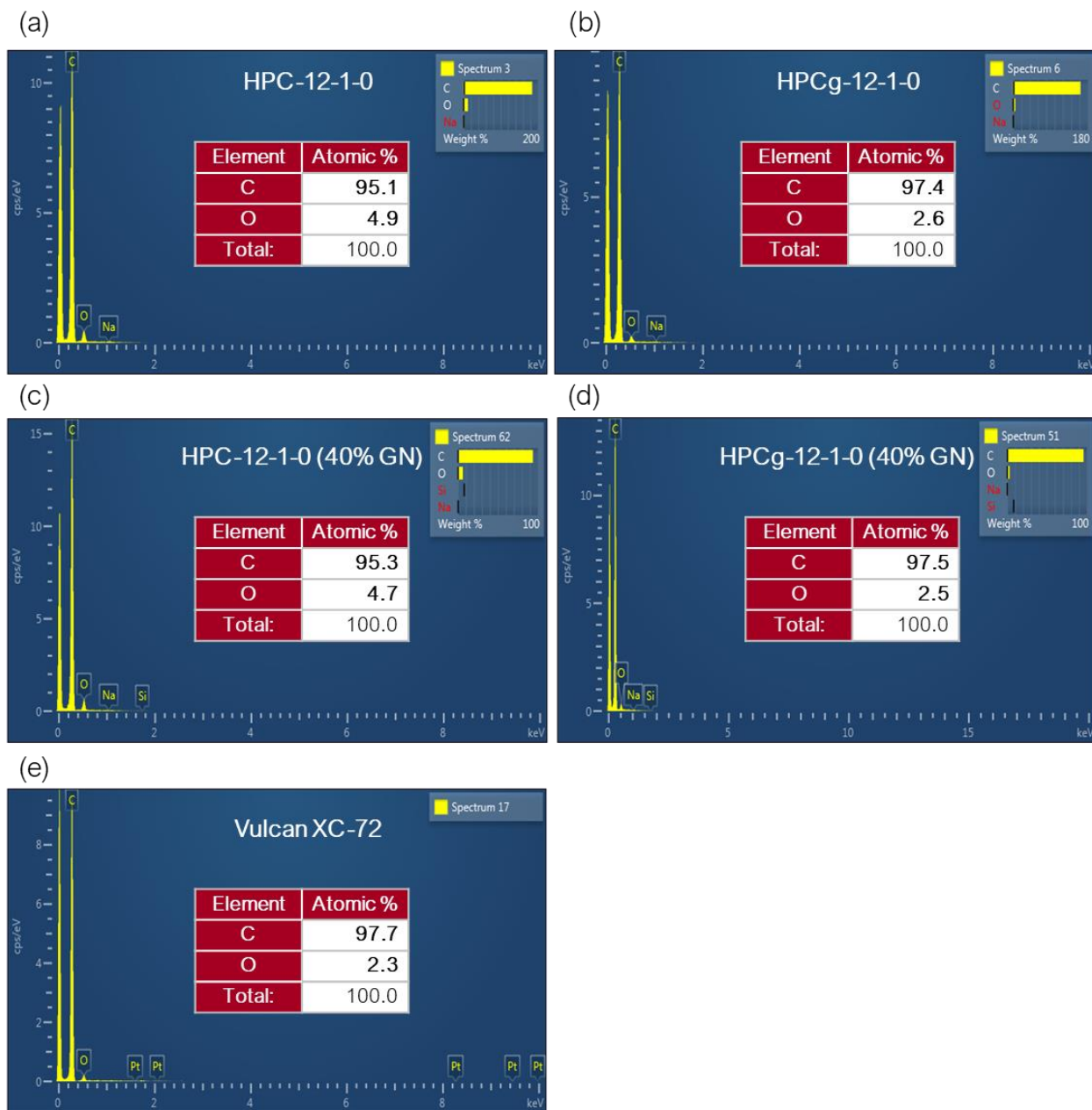


**Figure 3.9:** EDS results and atomic percentage of HPC-12-1-0 (pristine) and HPC-12-1-0 (40% GN). Vulcan XC-72 is included for comparison. (a) HPC-12-1-0 (pristine) (b) HPCg-12-1-0 (pristine) (c) HPC-12-1-0 (40% GN) (d) HPCg-12-1-0 (40% GN) (e) Vulcan XC-72.

## REFERENCES

- [1] S. Pérez-Rodríguez, D. Torres, M. J. Lázaro, *Powder Technol.* **2018**, *340*, 380.
- [2] T. W. Ebbesen, H. J. Lezec, H. Hiura, J. W. Bennett, H. F. Ghaemi, T. Thio, *Nature* **1996**, *382*, 54.
- [3] K. Kaneto, M. Tsuruta, G. Sakai, W. Y. Cho, Y. Ando, *Synth. Met.* **1999**, *103*, 2543.
- [4] J. C. Charlier, J. P. Issi, *J. Phys. Chem. Solids* **1996**, *57*, 957.
- [5] J. Sánchez-González, A. MacÍas-García, M. F. Alexandre-Franco, V. Gómez-Serrano, *Carbon N. Y.* **2005**, *43*, 741.
- [6] B. Marinho, M. Ghislandi, E. Tkalya, C. E. Koning, G. de With, *Powder Technol.* **2012**, *221*, 351.
- [7] T. M. Sun, L. M. Dong, C. Wang, W. L. Guo, L. Wang, T. X. Liang, *New Carbon Mater.* **2013**, *28*, 349.
- [8] D. Pantea, H. Darmstadt, S. Kaliaguine, L. Sümchen, C. Roy, *Carbon N. Y.* **2001**, *39*, 1147.
- [9] V. Celorrio, D. Sebastián, L. Calvillo, A. B. García, D. J. Fermin, M. J. Lázaro, *Int. J. Hydrogen Energy* **2016**, *41*, 19570.
- [10] D. Pantea, H. Darmstadt, S. Kaliaguine, C. Roy, *Appl. Surf. Sci.* **2003**, *217*, 181.
- [11] L. Estevez, R. Dua, N. Bhandari, A. Ramanujapuram, P. Wang, E. P. Giannelis, *Energy Environ. Sci.* **2013**, *6*, 1785.
- [12] R. Sahore, B. D. A. Levin, M. Pan, D. A. Muller, F. J. DiSalvo, E. P. Giannelis, *Adv.*

*Energy Mater.* **2016**, 6, 1.

## CHAPTER 4

### **STUDY OF ELECTROCATALYST SUPPORTED ON HPCs WITH DIFFERENT MESOPORE SIZE AND HPCs-GN COMPOSITES**

As mentioned in Section 1.1.1, exploration of novel carbon supports to further improve the utilization of electrocatalysts remains a vital issue in fuel cell related research. In this chapter, the goal is to evaluate the efficacy of HPCs with different mesopore size and HPCs-GN composites as catalyst supports by synthesizing Pt supported on HPCs (Pt/HPCs), and compare them with the commercial standard Pt supported on Vulcan XC-72 (Pt/C). The ultimate goals are to 1) understand how mesopore size will affect Pt nanoparticle dispersion and 2) evaluate HPCs-GN composites in terms of catalyst dispersion and benchmark them against Vulcan XC-72.

#### **4.1 Introduction**

For the deposition of electrocatalyst nanoparticles onto carbon supports, various methods including impregnation<sup>[1,2]</sup>, polyol<sup>[3]</sup>, sputter<sup>[4]</sup>, ultrasound<sup>[5]</sup>, microemulsion<sup>[6]</sup>, colloidal<sup>[7]</sup>, electrochemical<sup>[8]</sup>, and ion-exchange deposition<sup>[9]</sup> have been widely explored.<sup>[10]</sup> I will briefly introduce some of the common deposition techniques in the following paragraphs.

The impregnation method is currently the simplest way to prepare supported electrocatalyst. With this method, the support is immersed in a solution containing the metal precursor, and the capillary forces generated by the pores from the support facilitate dispersion. The above mixture is then set aside for hours to ensure equilibrium of the precursor distribution. Followed by drying and

chemical reduction (e.g. hydrogen reduction), the supported electrocatalyst is fabricated. This method is also known as conventional wet impregnation. However, during the process of evaporation and drying, the solvent will move within the absorbed layer, disturbing the distribution of metal precursor. Especially for porous supports, the capillary pressure difference will drive the solvent transport to the external surface, leading to aggregation of dissolved metal ions on the external surface. After drying and calcination, the poor metal dispersion and metal-support interactions undermine the resulting material properties when used as supported electrocatalysts in a fuel cell. Freeze-drying impregnation is thus devised to address the issue caused by wet impregnation. With the solvent solidified during the freezing process, the mobility of metal precursor is significantly reduced. The removal of solvent via sublimation can occur without pronounced aggregation of metal nanoparticles. The resulting supported electrocatalyst features enhanced metal-support interaction, leading to improved cell performance when compared with that synthesized by wet impregnation.<sup>[2]</sup>

To provide more adequate control over particle size and distribution than impregnation methods, alternative routes including colloidal methods using various stabilizing agents have been developed for preparing supported electrocatalysts. A stabilizing agent was utilized to prevent the aggregation of metal particles during the nucleation and growth stages. This stabilizing agent was usually removed by additional heat treatment, which inevitably resulted in sintering, affecting the phase separation and the distribution of metal particles. In this context, preparation via polyol method is preferred. The polyol method utilizes a polyol such as ethylene glycol as both solvent and reducing agent, and the polyol process does not require any additional polymer stabilizer. In the polyol process using ethylene glycol, metal ions are reduced to their neutral state by oxidizing ethylene glycol to glycolic acid. Glycolic acid exists in a deprotonated form as glycolate anion in

alkaline solution and acts as a stabilizer by adsorbing to the metal colloids. Thermal treatment as low as 160 °C to remove the organics from the metal surface has been reported, which is low enough to avoid detrimental effects on supported electrocatalysts associated with typical thermal treatment.<sup>[11]</sup>

Considering the nature of highly porous HPCs and HPCs-GN, the freeze-drying impregnation method was adopted to fabricate supported electrocatalysts.

## **4.2 Experimental Section**

### **4.2.1 Materials**

Chloroplatinic acid solution (8 wt%) was purchased from Sigma-Aldrich. 40 wt% Pt on Vulcan XC-72 was purchased from Fuel Cell Store.

### **4.2.2 Electrocatalyst Deposition on HPCs with Different Mesopore Size and HPCs-GN Composites**

To fabricate a 40 wt% Pt/HPCs-GN electrocatalyst, 1.44 mL chloroplatinic acid was added to 10 mL DI water in a 50 mL centrifugation tube. 200 mg HPCs-GN composite was then added to the mixing solution and the tube was sonicated for 10 mins to facilitate particle suspension. To achieve thorough mixing, an automated shaker was used at 300 rpm for 20 mins. The precursor mixture was then dipped into liquid nitrogen until solidified. A freeze dryer was used to sublime off ice



crystals for 3 days. The precursor mixture after freeze-drying was transferred to a crucible and loaded to the furnace. The mixture was heated at 225 °C under a constant flow of 6% H<sub>2</sub>/94% N<sub>2</sub> at a heating rate of 2 °C/min for 2 hours. The final product was then collected for further characterization. To synthesize Pt supported on HPCs with different mesopore size, the above procedure was repeated respectively with HPCg-4-1-0 (pristine), HPCg-12-1-0 (pristine), and HPCg-20-1-0 (pristine) as starting materials.

### **4.3 Characterization**

The surface morphology, microstructure, and chemical composition of samples were investigated by scanning electron microscopy (SEM) and energy dispersive X-ray spectroscopy (EDS) using Zeiss Gemini 500 Scanning Electron Microscope with operating voltages between 1-5 keV. Nitrogen adsorption isotherms of samples were recorded on Micromeritics ASAP 2460 analyzer at 77 K. The Brunauer-Emmett-Teller (BET) model was used to calculate specific surface areas of the samples. The Barrett-Joyner-Halenda (BJH) model was applied to obtain pore size distributions and total pore volumes of samples from the adsorption branch of isotherms. Elemental composition and electronic structure were analyzed from X-ray photoelectron spectroscopy (XPS) using ESCA 2SR XPS with operating pressures of 10<sup>-9</sup> Torr. The samples in powder form were deposited on copper tape. Survey and high sensitivity spectra were collected at 200 eV pass energy, and high resolution at 50 eV pass energy. Thermogravimetric analysis (TGA) measurements were performed in air with a heating rate of 5 °C/min till 900 °C on TA Instruments Q500 Thermogravimetric Analyzer.

## 4.4 Results and Discussions

### 4.4.1 Thermogravimetric Results for Electrocatalyst Loading Quantification of Pt-supported on HPCs with Different Mesopore Size and HPCs-GN Composites

Figure 4.1 demonstrates the TGA results of Pt supported on HPCs with different mesopore size, HPCs-GN, and Vulcan XC-72. While the TGA measurements conducted in air for Pt/HPCs and Pt/Vulcan XC-72 have similar results to those in nitrogen, in terms of Pt quantification, measurements in air in which the carbon materials have lower decomposition temperature are preferred and were performed. All supported electrocatalysts exhibited subtle weight loss below 100 °C. This was due to the evaporation of water absorbed by the materials. When the temperature reached around 300 °C, a sharp weight decrease occurred for all supported electrocatalysts, corresponding to the decomposition temperature of carbon. The mesopore size in HPCs does not appear to significantly affect the decomposition temperature. However, for Pt/HPCs-GN, there was another sharp decrease at 400 °C, indicating there were two stages of decomposition with respect to Pt/HPCs-GN. Considering the graphitic structure of graphene nanoplatelets leading to a higher decomposition temperature than amorphous carbon, the first stage of weight loss was attributed to the decomposition of HPCs and the later stage to the decomposition of graphene nanoplatelets. With graphene nanoplatelets in the composite, the decomposition process became broader spanning a wider temperature range. The decomposition was completed at 700 °C. The remaining material is Pt metal with a melting point over 1500 °C. The weight percentage of Pt for all supported electrocatalysts after TGA measurement was around 40 wt% with a deviation less than 5%. For all supported electrocatalysts, the slight weight gain after full decomposition of

carbon materials was due to the metal oxide formation, since the measurements were performed in air.

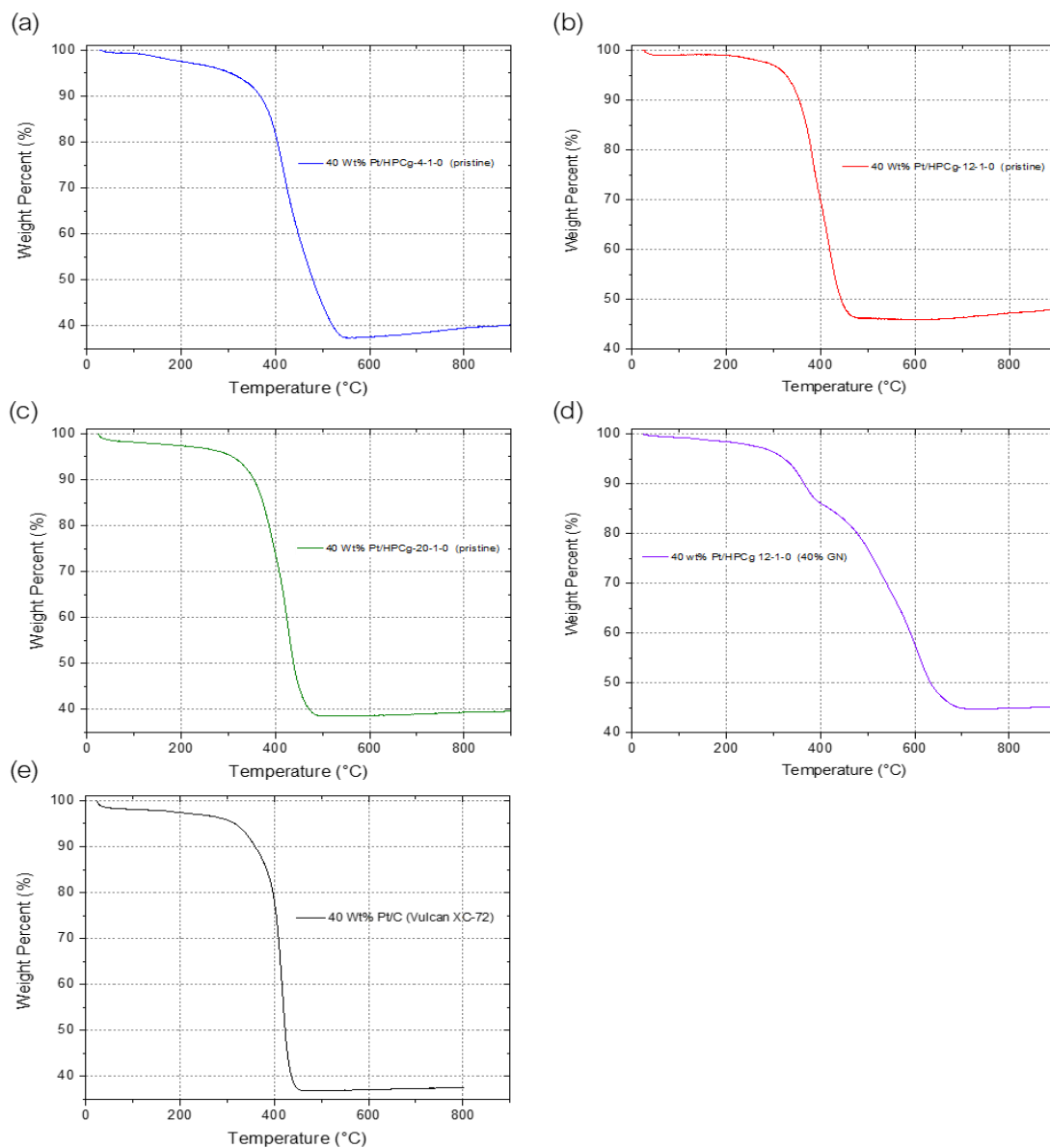


**Figure 4.1:** TGA results of supported electrocatalysts. (a) 40 wt% Pt/HPCg-4-1-0 (pristine) (b) 40 wt% Pt/HPCg-12-1-0 (pristine) (c) 40 wt% Pt/HPCg-20-1-0 (pristine) (d) 40 wt% Pt/HPCg-12-1-0 (40% GN) (e) commercial 40 wt% Pt/Vulcan XC-72.

#### **4.4.2 Nanoparticle Size Distribution of Pt-supported on HPCs with Different Mesopore Size and HPCs-GN Composites**

As mentioned in Section 1.1.1, the ultimate goal for the exploration of novel carbon supports is to improve the utilization of electrocatalysts. To this end, one of the key parameters is the size of catalyst nanoparticles deposited because smaller particles could provide more active sites, resulting in enhanced fuel cell performance. SEM images were taken to evaluate the size of Pt nanoparticles on HPCs with different mesopore size, HPCs-GN composite, and Vulcan XC-72.

Figure 4.2 shows the high-resolution SEM images of Pt supported on different carbon supports. Small Pt nanoparticles could be distinguished from the carbon substrates, especially for Vulcan XC-72 which features a spherical and smooth surface. Due to the porous structure of HPCs and HPCs-GN composite, it is possible to mistake the surface morphology for Pt nanoparticles. While the SEM images mentioned above were taken and reconstructed with secondary electron signal, we also took images using back-scattered electron (BSE) signal, which is sensitive to high atomic number element including Pt and would exhibit strong contrast between high and low atomic number elements. This approach benefits particle size calculation owing to improved accuracy.

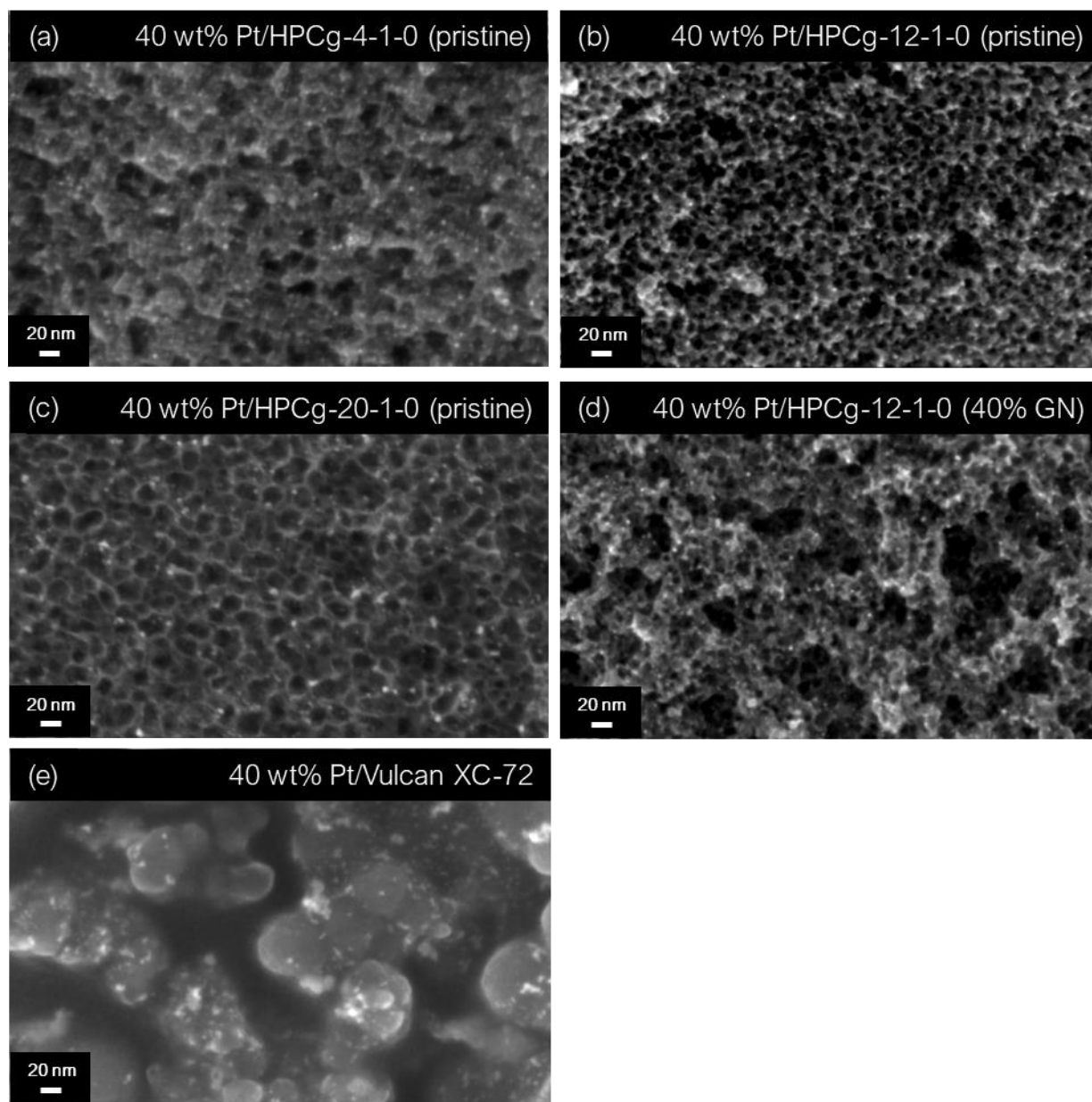


**Figure 4.2:** SEM images of Pt supported on different carbon supports. (a) 40 wt% Pt/HPCg-4-1-0 (pristine) (b) 40 wt% Pt/HPCg-12-1-0 (pristine) (c) 40 wt% Pt/HPCg-20-1-0 (pristine) (d) 40 wt% Pt/HPCg-12-1-0 (40% GN) (e) commercial 40 wt% Pt/Vulcan XC-72.

Figure 4.3 demonstrates the BSE images taken at the same spot of Figure 4.2, and the particle size distribution (PSD) diagrams calculated based on the BSE images are shown together. From the BSE images, it can be clearly seen that the Pt nanoparticles were homogeneously distributed on

all HPCs and HPCs-GN composites. For quantitative analysis, I performed Pt nanoparticle size calculations using these images. From the PSD diagrams, it can be inferred that 40 wt% Pt/HPCg-4-1-0 (pristine), 40 wt% Pt/HPg-12-1-0 (pristine), and 40 wt% Pt/HPCg-12-1-0 (40% GN) have a smaller mean Pt nanoparticle size around 4 – 5 nm compared with 40 wt% Pt/HPCg-20-1-0 (pristine), which has a mean Pt particle size around 8 nm, similar to that of 40 wt% Pt/Vulcan XC-72. The particle size distributions were also more uniform for the former samples.

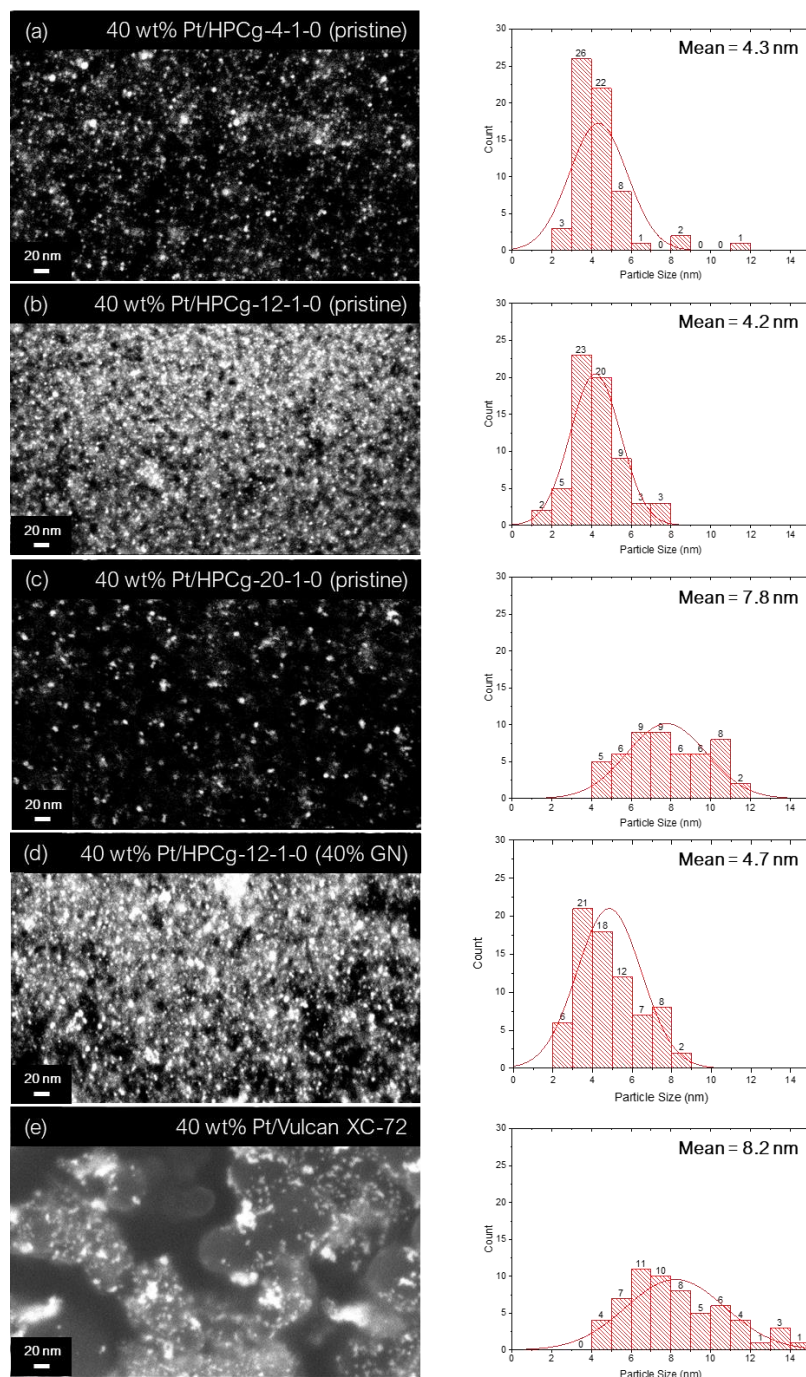


**Figure 4.3:** BSE images of Pt supported on different carbon supports and the resulting Pt PSD diagrams. (a) 40 wt% Pt/HPCg-4-1-0 (pristine) (b) 40 wt% Pt/HPCg-12-1-0 (pristine) (c) 40 wt% Pt/HPCg-20-1-0 (pristine) (d) 40 wt% Pt/HPCg-12-1-0 (40% GN) (e) commercial 40 wt% Pt/Vulcan XC-72. The fitting curve in each PSD diagram is included based on the histogram.

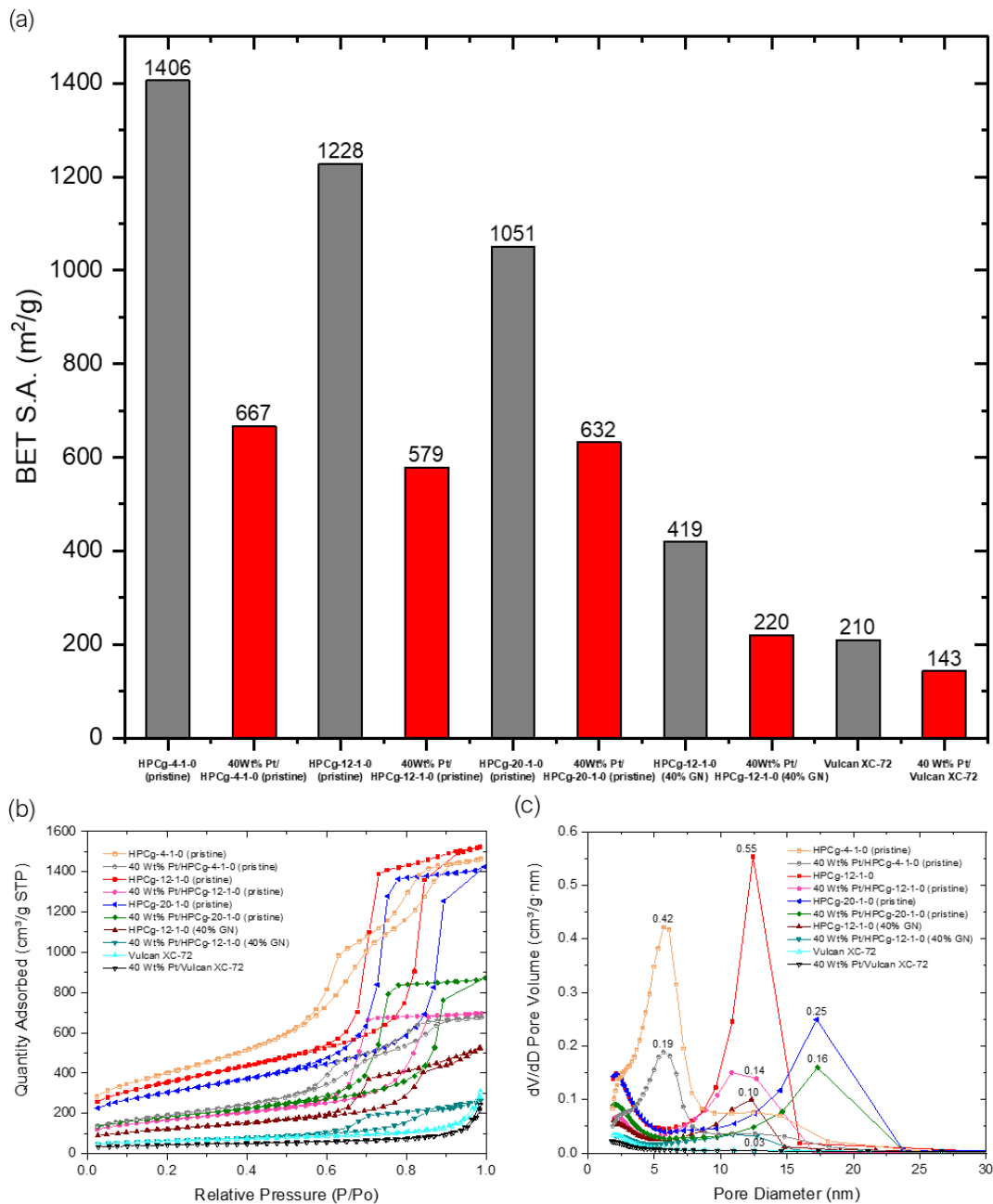
#### 4.4.3 Structural Investigation after Pt deposition

Figure 4.4 (a) contains the surface area values of HPCs before and after electrocatalyst deposition measured by nitrogen adsorption. For HPCs and HPC-GN composite, the surface area decreases to about half after electrocatalyst deposition. However, the surface area values for both Pt/HPCs with different mesopore size and Pt/HPCs-GN are still higher than that of Pt/Vulcan XC-72. Quantitative analysis of pore volume summarized in Table 4.1 suggested that the pore volume for both mesopore and micropore decreased to half after Pt deposition. Adsorption isotherms and pore size distribution are presented in Figure 4.4 (b) and (c). From the isotherms, the shrinkage of hysteresis for samples with Pt deposition indicated decreased mesoporosity. It can be concluded from the pore size distribution diagrams that mesopore volume significantly decreased after Pt deposition, but the majority of pores were still mesopores for the Pt/HPCs samples, and the mesopore size distribution before and after Pt deposition remained similar for HPCs with different mesopore size and HPCs-GN composite. The feature of highly uniform mesopore size for HPCs systems was retained after Pt deposition. Nitrogen adsorption results of Vulcan XC-72, featuring a high percentage of micropores, before and after Pt deposition were also provided for comparison. After Pt deposition, the micropore volume of Vulcan XC-72 was also decreased, but the extent of decrease was not as pronounced as in the HPCs samples.



**Table 4.1:** Pore volume of HPCs with different mesopore size and HPCs-GN before/after Pt deposition. Vulcan XC-72 before and after Pt deposition are included for comparison.

<b>Sample</b>	<b>V<sub>meso</sub> (cm<sup>3</sup>/g)</b>	<b>V<sub>micro</sub> (cm<sup>3</sup>/g)</b>	<b>Sample</b>	<b>V<sub>meso</sub> (cm<sup>3</sup>/g)</b>	<b>V<sub>micro</sub> (cm<sup>3</sup>/g)</b>
<b>HPCg-4-1-0 (pristine)</b>	2.33	0.080	<b>40 wt% Pt/ HPCg-4-1-0 (pristine)</b>	1.08	0.038
<b>HPCg-12-1-0 (pristine)</b>	2.35	0.108	<b>40 wt% Pt/ HPCg-12-1-0 (pristine)</b>	1.11	0.050
<b>HPCg-20-1-0 (pristine)</b>	1.89	0.109	<b>40 wt% Pt/ HPCg-20-1-0 (pristine)</b>	1.16	0.057
<b>HPCg-12-1-0 (40% GN)</b>	0.81	0.034	<b>40 wt% Pt/ HPCg-12-1-0 (40% GN)</b>	0.42	0.017
<b>Vulcan XC-72</b>	0.40	0.032	<b>40 wt% Pt/ Vulcan XC-72</b>	0.32	0.022



**Figure 4.4:** (a) BET surface area comparison of HPCs with different mesopore size and HPCs-GN, before and after Pt deposition (b) isotherms of HPCs with different mesopore size and HPCs-GN, before and after Pt deposition (c) pore size distribution of HPCs with different mesopore size and HPCs-GN, before and after Pt deposition. Vulcan XC-72 before and after Pt deposition are included for comparison.

## REFERENCES

- [1] X. Li, I. M. Hsing, *Electrochim. Acta* **2006**, 51, 5250.
- [2] L. Fan, D. Cheng, F. Chen, X. Zhan, *Chinese J. Catal.* **2019**, 40, 1109.
- [3] S. L. Knupp, W. Li, O. Paschos, T. M. Murray, J. Snyder, P. Haldar, *Carbon N. Y.* **2008**, 46, 1276.
- [4] S. Mukerjee, S. Srinivasan, A. J. Appleby, *Electrochim. Acta* **1993**, 38, 1661.
- [5] D. Nagao, Y. Shimazaki, S. Saeki, Y. Kobayashi, M. Konno, *Colloids Surfaces A Physicochem. Eng. Asp.* **2007**, 302, 623.
- [6] M. Boutonnet, J. Kizling, P. Stenius, G. Maire, *Colloids and Surfaces* **1982**, 5, 209.
- [7] T. Yoshitake, Y. Shimakawa, S. Kuroshima, H. Kimura, T. Ichihashi, Y. Kubo, D. Kasuya, K. Takahashi, F. Kokai, M. Yudasaka, S. Iijima, *Phys. B Condens. Matter* **2002**, 323, 124.
- [8] T. M. Day, P. R. Unwin, N. R. Wilson, J. V. Macpherson, *J. Am. Chem. Soc.* **2005**, 127, 10639.
- [9] K. Yasuda, Y. Nishimura, *Mater. Chem. Phys.* **2003**, 82, 921.
- [10] S. Sharma, B. G. Pollet, *J. Power Sources* **2012**, 208, 96.
- [11] A. Esmaeilifar, S. Rowshanzamir, M. H. Eikani, E. Ghazanfari, *Energy* **2010**, 35, 3941.